



Citation for published version:

Cox, J 2020, 'The Functional Nasal Anatomy of the Pike, *Esox lucius* L.', *Comparative Biochemistry and Physiology - Part A: Molecular & Integrative Physiology*, vol. 244, 110688.
<https://doi.org/10.1016/j.cbpa.2020.110688>

DOI:

[10.1016/j.cbpa.2020.110688](https://doi.org/10.1016/j.cbpa.2020.110688)

Publication date:

2020

Document Version

Peer reviewed version

[Link to publication](#)

Publisher Rights

CC BY-NC-ND

University of Bath

Alternative formats

If you require this document in an alternative format, please contact:
openaccess@bath.ac.uk

General rights

Copyright and moral rights for the publications made accessible in the public portal are retained by the authors and/or other copyright owners and it is a condition of accessing publications that users recognise and abide by the legal requirements associated with these rights.

Take down policy

If you believe that this document breaches copyright please contact us providing details, and we will remove access to the work immediately and investigate your claim.

1 **The Functional Nasal Anatomy of the Pike, *Esox lucius* L.**

2
3 Russell J. Garwood^a, Julia Behnsen^b, Andrew T. Ramsey^c, Harriet K. Haysom^d, Luke J.
4 Dalby^e, Samuel K. Quilter^e, James S. Maclaine^f, Zhijin Wang^g, Jonathan P. L. Cox^d

5
6 *^aDepartment of Earth and Environmental Sciences, University of Manchester, Manchester,*
7 *M13 9PL, UK*

8 *^bHenry Moseley X-ray Imaging Facility, University of Manchester, Manchester, M13 9PY,*
9 *UK*

10 *^cNikon Metrology, 12701 Grand River Avenue, Brighton, MI 48116, USA*

11 *^dDepartment of Chemistry, University of Bath, Bath, BA2 7AY, UK*

12 *^eTotalSim, Top Station Road, Brackley, NN13 7UG, UK*

13 *^fDepartment of Life Sciences, Natural History Museum, Cromwell Road, London, SW7 5BD,*
14 *UK*

15 *^gDepartment of Mechanical Engineering, University of Bath, Bath, BA2 7AY, UK*

16
17
18 **MS has 55 pages, 17 figures, 1 video, 1 appendix**

19
20 **Declaration of interest: None**

21
22 *Corresponding author

23 Dr Jonathan P.L. Cox

24 Department of Chemistry

25 University of Bath

26 Bath, BA2 7AY, UK

27 Tel. +44 1225 386548

28 j.p.l.cox@bath.ac.uk

29 **Abstract**

30 Olfactory flow in fishes is a little-explored area of fundamental and applied importance. We
31 investigated olfactory flow in the pike, *Esox lucius*, because it has an apparently simple and
32 rigid nasal region. We characterised olfactory flow by dye visualisation and computational
33 fluid dynamics, using models derived from X-ray micro-computed tomography scans of two
34 preserved specimens. An external current induced a flow of water through the nasal chamber
35 at physiologically relevant Reynolds numbers (200 – 300). We attribute this externally-
36 induced flow to: the location of the incurrent nostril in a region of high static pressure; the
37 nasal bridge deflecting external flow into the nasal chamber; an excurrent nostril normal to
38 external flow; and viscous entrainment. A vortex in the incurrent nostril may be instrumental
39 in viscous entrainment. Flow was dispersed over the olfactory sensory surface when it
40 impacted on the floor of the nasal chamber. Dispersal may be assisted by: the radial array of
41 nasal folds; a complementary interaction between a posterior nasal fold and the ventral
42 surface of the nasal bridge; and the incurrent vortex. The boundary layer could delay
43 considerably (up to ~ 3 s) odorant transport from the external environment to the nasal
44 region. The drag incurred by olfactory flow was almost the same as the drag incurred by
45 models in which the nasal region had been replaced by a smooth surface. The boundary layer
46 does not detach from the nasal region. We conclude that the nasal bridge and the incurrent
47 vortex are pivotal to olfaction in the pike.

48

49 **Keywords:** Artificial chemical sensor; 3D printing; pressure coefficient; streamline;
50 sturgeon.

51

52 **1. Introduction**

53 The anatomy of a fish determines how water flows in and around its nasal region (Theisen,
54 1982). Olfactory flow in turn determines how odorants are transported to the olfactory
55 epithelium (Zeiske et al., 1992; Cox, 2008). Effective odorant transport requires flow through
56 the fish's nasal chamber (Cox, 2008), and dispersal of flow over the olfactory epithelium
57 (Holmes et al., 2011). But odorant transport must contend with the presence of a boundary
58 layer on the surface of the fish (Denny, 1993, p. 138-140; Cox, 2008). Furthermore, olfactory
59 flow will incur drag, and so exact a metabolic cost.

60

61 Here we report the functional nasal anatomy of the pike, *Esox lucius* (Esocidae; Nelson,
62 2006, p. 205). We chose the pike, a predatory fish that occupies a wide range of habitats
63 (Craig, 2008), for the following reasons. First, its nasal anatomy appears simple (Fig. 1C – F;
64 Burne, 1909; Holl, 1965). Second, its nasal anatomy suggests that flow of water through the
65 nasal chamber may be induced by an external flow (Burne, 1909; Cox, 2008), i.e. by the fish
66 moving forward, and/or by an environmental water current. Raat (1988, p. 52) in fact states
67 that water flows through the nasal chamber only when the pike moves, although there is no
68 evidence for this claim in the reference he cites (Devitsina and Malyukina, 1977). Third, the
69 nasal region appears rigid, and so may be faithfully represented by a rigid plastic model.
70 Finally, there are no moving macroscopic parts in the nasal region to complicate olfactory
71 flow.

72

73 We investigated the functional nasal anatomy of the pike by addressing the following
74 questions. 1) Can flow through the nasal chamber be induced by an external flow? 2) If so,
75 how? 3) How is flow dispersed over the olfactory epithelium? 4) How does the boundary
76 layer influence odorant transport? 5) What drag does the nasal region incur? Boundary layers
77 and drag have been mentioned before in relation to olfactory flow in fishes (Cox, 2008;
78 Agbesi et al., 2016a, 2016b), but not quantified.

79

80 We tackled these questions using the complementary techniques of dye visualisation and
81 computational fluid dynamics (Garwood et al., 2019). The anatomically-accurate models
82 employed in our experiments were derived from X-ray micro-computed tomography scans of
83 two well-preserved specimens whose nasal anatomy differs in several important age-related
84 respects. We compare the results from the models of both specimens. We also compare
85 olfactory flow in the pike with that in the sturgeon. We do so because the sturgeon's nasal

86 region is like that of the pike (Cox, 2008), and because flow through the nasal chamber of the
87 sturgeon is externally-induced (Garwood et al., 2019). Readers unfamiliar with fluid
88 dynamics are referred to Shapiro (1961) and Vogel (1994).

89 **2. Materials and methods**

90 Most of the methodology used here has been described before (Cox, 2008; Abel et al., 2010;
91 Holmes et al., 2011; Howard et al., 2013; Ramsey et al., 2015; Garwood et al., 2019). We
92 therefore give only brief descriptions here. Further details are given in the Appendix. Values
93 for the density and dynamic viscosity of water are taken from Haynes and Lide (2011, p. 6-
94 7), and Table 1 of Goldstein (1965), respectively.

95

96 *2.1. Preserved specimens*

97 The two preserved specimens of the pike, *Esox lucius* (Fig. 1), used to construct the models
98 are from the Natural History Museum, London, UK. The first specimen (catalogue number
99 BMNH 1963.4.26.2), which we refer to as the juvenile pike, was caught by dip net on 19
100 August 1962 at the mouth of the Kandik River, Alaska, USA. The second specimen
101 (catalogue number BMNH 1986.5.20.4), which we refer to as the adult pike, was caught
102 (method of capture not recorded) on 7 May 1986 in the Mill Stream, East Stoke, Dorset, UK.
103 The fork lengths (Fig. 1A, *FL*; Fig. 2.2 of Helfman et al., 2009) and wet weights of the
104 specimens are 18.5 cm and 40 g (juvenile pike), and 34 cm and 380 g (adult pike). The fork
105 lengths of the specimens indicate that they were about one year old (juvenile pike) and two
106 years old (adult pike) when caught (Table 4.1 of Craig, 1996). Since capture, both specimens
107 have been stored in 70 % industrial methylated spirits, 30 % distilled water.

108

109 *2.2. In vivo observations*

110 Four pike (*FL* ~ 75 – 100 cm) were observed *in vivo* at the Aquarium of the Lakes, Cumbria,
111 UK, 4 – 5 June 2015. We refer to these specimens as the aquarium specimens. The nasal
112 anatomy of 11 additional specimens (*FL* = 10 – 50 cm) was observed *in vivo* (but with the
113 specimens temporarily out of water) during a joint Environment Agency/University of
114 Bournemouth (both UK) survey at Tewkesbury and Upton Marinas, River Severn, UK, on 22
115 June 2017. (We did not participate in this survey.) The 11 specimens, which we refer to as the
116 survey specimens, were captured by seine net and, following observation, returned to the
117 water alive. Regulated procedures completed on the survey specimens were performed by
118 Environment Agency/University of Bournemouth personnel under UK Home Office licence
119 70/8063 and after ethical review.

120

121 *2.3. X-ray micro-computed tomography*

122 X-ray micro-computed tomography (micro-CT) of the preserved specimens was done at
123 Nikon Metrology, Tring, UK (juvenile pike) and at the Henry Moseley X-ray Imaging
124 Facility, University of Manchester, UK (adult pike) using an XT H 225 system. Both scans
125 were performed in air. The scan of the juvenile pike comprised 1807 TIFF images (e.g. Fig.
126 2A) and had a voxel size of $29\ \mu\text{m} \times 29\ \mu\text{m} \times 29\ \mu\text{m}$ ([dataset] Ramsey et al., 2019). The
127 scan of the adult pike comprised 1772 TIFF images (e.g. Fig. 2B) and had a voxel size of 52
128 $\mu\text{m} \times 52\ \mu\text{m} \times 52\ \mu\text{m}$ ([dataset] Garwood et al., 2020). Both scans extended from the rostral
129 tip to the gill region (Fig. 1C and D). Further details of the scans are given in Appendix
130 A.1.1.

131

132 *2.4. Surface models*

133 Surface models of the heads of the juvenile and adult pike were generated with the image
134 processing software ScanIP (Synopsys, Mountain View, USA) as previously described
135 (Garwood et al., 2019). We prepared two types of surface model: ‘wild type’ models (Fig. 3;
136 [dataset] Haysom et al., 2020), in which the nasal regions of the model were intact, and
137 ‘mutant’ models (Fig. A.7, Appendix A.5; [datasets] Haysom et al., 2020), in which the
138 nostrils and nasal chamber of each nasal region were replaced by a continuous surface that
139 blended smoothly with the rest of the head. The mutant models were used in the CFD
140 simulations, specifically for the drag calculations, and to investigate the boundary layer in the
141 nasal region (Section 2.7). Unless otherwise stated, any reference to a surface model is to the
142 wild type model. Further details of the surface models are given in Appendix A.1.2 and
143 A.1.7.4.

144

145 *2.5. Plastic models*

146 The plastic models of the heads (both wild type; Fig. 4) were either 3x (juvenile pike) or 2x
147 (adult pike) life size. The plastic models were larger than life to allow us to see clearly dye
148 behaviour in the nasal region (Section 2.6). Fabrication and assembly of the models are
149 described in Appendix A.1.3.

150

151

152 2.6. Dye visualisation

153 Dye visualisation was performed in an Eidetics Model 1520 closed-circuit, free-surface,
154 continuous-flow flume (Wang et al., 2007) using the plastic models of the juvenile and adult
155 pike heads. To obtain a well-defined dye filament, we operated the flume at a free-stream
156 speed of 5 cm s^{-1} . This speed corresponded to Reynolds numbers of 200 – 300 for both
157 models (Section 2.9.2), a range indicative of laminar flow (Vogel, 1994, pp. 84-85).
158 According to the principle of dynamic similarity (Shapiro, 1961, p. 74; Vogel, 1994, p. 102),
159 a speed of 5 cm s^{-1} with the 3x life-sized model of the juvenile pike corresponds to a free-
160 stream speed of 15 cm s^{-1} for the actual specimen, or 0.8 FL s^{-1} ($FL = 18.5 \text{ cm}$; Section 2.1).
161 Similarly, a speed of 5 cm s^{-1} with a 2x life-sized model of the adult pike corresponds to a
162 free-stream speed of 10 cm s^{-1} for the actual specimen, or 0.3 FL s^{-1} ($FL = 34 \text{ cm}$; Section
163 2.1). These free-stream speeds fall into the range of environmental currents ($\leq 30 \text{ cm s}^{-1}$) and
164 swimming speeds ($0.08 - 4 \text{ FL s}^{-1}$) a stationary/cruising pike may encounter/adopt (Appendix
165 A.1.4 and A.1.5; Webb, 1984). We therefore consider Reynolds numbers of 200 – 300 to be
166 physiologically relevant.

167

168 The pitch and yaw (Fig. 10.1 of Barnard and Philpott, 2004) of the plastic models were both
169 0° . Roll angles (ibid.) are specified in the legends for the video clips. Flow was visualised
170 with red food dye diluted in a ratio of four parts water to one part dye. The water temperature
171 in the flume varied between $12 - 16.5 \text{ }^\circ\text{C}$, and changed by $\leq 2.5 \text{ }^\circ\text{C}$ in a single day. Dye
172 visualisation experiments were recorded on a Panasonic HC-V500 digital camcorder (50
173 frames s^{-1} , $1920 \text{ pixels} \times 1080 \text{ pixels}$ per frame) mounted on a Velbon DV-7000 tripod fitted
174 with a Vel-flo 9 PH-368 head. Footage was analysed using the software Adobe Premiere Pro
175 CC. Further details of the dye visualisation experiments are given in Appendix A.1.6.

176

177 2.7. Computational fluid dynamics

178

179 2.7.1. General

180 Computational fluid dynamics (CFD) simulations of olfactory flow in the pike were
181 performed on life-sized models of both the juvenile and the adult pike. The simulations were
182 run using the software OpenFOAM (Weller et al., 1998). The surface of each CFD mesh was
183 refined in the nasal region (Fig. 5A). Adjacent to the surface of the nasal region, the mesh

184 comprised five layers of cells (Fig. 5C, inset). The thickness of these cells was sufficient to
185 capture the velocity gradients here. The number of cells across the nasal passage was 40 – 50
186 (e.g. Fig. 5C). Simulations were run at inlet velocities of 15 cm s⁻¹ (juvenile pike) and 10 cm
187 s⁻¹ (adult pike), corresponding to Reynolds numbers of 200 – 300 (Section 2.9.3), and
188 therefore matching the Reynolds numbers for the dye visualisation experiments (Section 2.6).
189 Pitch and roll were 0°; yaw was 0 ± 5° (positive and negative yaw angles are indicated in Fig.
190 3A). Simulations in which yaw was varied were only performed for the wild type models. For
191 a particular simulation, the density and dynamic viscosity were set to either: 999.2 kg m⁻³ and
192 1.2 x 10⁻³ Pa s; or 999.1 kg m⁻³ and 1.1 x 10⁻³ Pa s (values for water at 14 and 15 °C,
193 respectively). Flow was assumed to be steady, laminar (Section 2.6), isothermal, and
194 incompressible. The assumption of steady flow was based on initial transient simulations. In
195 the transient simulation for the juvenile pike, the static pressure in the centre of both types of
196 nostril (incurrent and excurrent) was found over 4 s to vary by < 0.03 % of the average static
197 pressure at these locations over that time period (Fig. A.6, double-asterisked line, Appendix
198 A.5). In the transient simulation for the adult pike, the flow rate through a plane of refined
199 cells in each nostril (e.g. Fig. 5C of Garwood et al., 2019) was found over 12 s to vary by <
200 0.02 %. Velocities, static pressures, and shear stresses were the averages of the last 500
201 iterations from a total of 2000 iterations of a converged, time-averaged solution to the
202 Navier-Stokes equations. Convergence was checked by monitoring the volumetric flow rate
203 through a plane of refined cells in each nostril of both the juvenile and the adult pike.
204 Because the volumetric flow rate through these planes changed by ≤ 0.03 % over the last 500
205 iterations of the simulations, we assumed convergence had occurred. Results from the CFD
206 simulations were analysed and visualised with ParaView (Ayachit, 2016). Full details are
207 given in Appendix A.1.7. Because flow was steady in the CFD simulations, the streamlines
208 generated in ParaView equate to pathlines (Kline, 1972), and therefore indicate the path a
209 fluid particle takes (Barnard, 2009, p. 6). Further details of the simulations are given in
210 Appendix A.1.7.1.

211

212 2.7.2. Pressure

213 Static pressures are expressed as pressure coefficients (C_p ; Douglas et al., 1985; Vogel,
214 1988), i.e. the ratio of the static pressure ($P - P_0$) to the dynamic pressure of the free-stream
215 flow ($\frac{1}{2}\rho U_0^2$):

216

217
218
219
220
221
222
223
224
225
226
227
228
229
230
231
232
233
234
235
236
237
238
239
240
241
242
243
244
245
246
247
248

$$C_p = \frac{P - P_0}{\frac{1}{2}\rho U_0^2}$$

Equation 1

where P is the static pressure at a given point, P_0 is the ambient static pressure of the fluid (set to zero in the CFD simulations), ρ is the density of the fluid (999.1 or 999.2 kg m⁻³; above), and U_0 is the free-stream speed (inlet velocity = 10 or 15 cm s⁻¹).

The fraction of the dynamic pressure of the free-stream flow harnessed by the nasal region (ΔC_p) was calculated using Equation 2:

$$\Delta C_p = C_p (\text{Incurrent nostril}) - C_p (\text{Excurrent nostril}) \quad \text{Equation 2}$$

where C_p (Incurrent nostril) and C_p (Excurrent nostril) are the average pressure coefficients for the fluid in the incurrent and excurrent nostrils, respectively. ΔC_p is given as a percentage in the ensuing text.

Details of how we located points of static pressure on the surface of a CFD model and of how we calculated the static pressure in each nostril are given in Appendix A.1.7.2.

2.7.3. Boundary layer

We gauged the thickness of the boundary layer on the surfaces of the model pike using vorticity (Abernathy, 1972; Thwaites, 1960, p. 18). (We did not use speed to gauge the boundary layer thickness because the contours of speed were not asymptotic in the nasal region; Fig. A.9C and D, Appendix A.5). We defined the thickness of the boundary layer using a vorticity of 5 s⁻¹. This value gave a contour within ParaView that was a) smooth and b) located in a similar position to the dorsal limit of the dye filament in the dye visualisation experiments involving the adult pike model (Section 3.2). Values less than 5 s⁻¹ gave noisier contours. Details of how we estimated the thickness of the boundary layer are given in Appendix A.1.7.5, together with details of how we estimated the time taken for a fluid particle to get from the point of entry into the boundary layer to the incurrent nostril.

249 2.7.4. *Drag*

250 Drag was estimated using the method described in Appendix A.1.7.6. The drag-related
251 figures given in Table 1 are for the two *combined* nasal regions.

252

253 2.8. *Morphometry*

254 Morphometric measurements (e.g. nasal chamber volumes) were made using ParaView,
255 Rhinoceros (Version 4.0, Robert McNeel & Associates), and ScanIP, according to previous
256 methodology (e.g. Garwood et al., 2019, Appendix A.1.5). Morphometric measurements
257 were made on both the left and right nasal regions.

258

259 2.9. *Reynolds numbers*

260

261 2.9.1. *General*

262 Reynolds numbers (Re) for olfactory flow were calculated using either Equation 3 (Vogel,
263 1994, p. 85) or Equation 4 (Holmes et al., 2011):

264

265
$$Re = \frac{UL\rho}{\mu}$$

266

Equation 3

267

268
$$Re = \frac{4Q\rho}{L\mu}$$

269

Equation 4

270

271 where U is the speed of the fluid, L is the characteristic dimension of the object, μ is the
272 dynamic viscosity of the fluid, and Q is the volumetric flow rate. For external olfactory flow,
273 U was the free-stream speed (U_0), and L was the width of the nasal region in dorsal profile,
274 normal to the direction of flow (Fig. 6B). For internal olfactory flow, L was the wetted
275 perimeter of the nasal chamber (Fig. 2A and B, yellow lines). Reynolds numbers are given to
276 one significant figure.

277

278 2.9.2. *Reynolds numbers for dye visualisation*

279 The Reynolds numbers for olfactory flow in the dye visualisation experiments were
280 calculated (Equation 3) with $U = 5 \text{ cm s}^{-1}$ (the free-stream speed in the flume; Section 2.6), L

281 = 6 mm (juvenile pike) or 7 mm (adult pike), $\rho = 998.9 - 999.5 \text{ kg m}^{-3}$, and $\mu = 1.1 - 1.2 \times$
282 10^{-3} Pa s at $12 - 16.5 \text{ }^\circ\text{C}$ (water temperature in the flume; Section 2.6).

283

284 *2.9.3. Reynolds numbers for CFD*

285 Calculations of Reynolds numbers for olfactory flow in the CFD simulations used the values
286 of speed (inlet velocity), density, and dynamic viscosity given in Section 2.7.1. Reynolds
287 numbers for olfactory flow were calculated (Equation 3) with $L = 1.9 \text{ mm}$ (juvenile pike) or
288 3.4 mm (adult pike). Reynolds numbers for flow through each nasal chamber were calculated
289 (Equation 4) with $Q = 10 \text{ mm}^3 \text{ s}^{-1}$ (juvenile pike) or $60 \text{ mm}^3 \text{ s}^{-1}$ (adult pike), and $L = 6 \text{ mm}$
290 (juvenile pike) or 12 mm (adult pike). Volumetric flow rates were determined according to
291 Appendix A.1.6 of Garwood et al. (2019). The slices used to determine each flow rate are
292 shown in Fig. 5C, and Fig. A.5C, Appendix A.5.

293

294 *2.10. Videos and figures*

295 In keeping with our work on the sturgeon (Garwood et al., 2019), the video clips (see Video,
296 Supplementary data) and figures are shown in the same orientation, with the anterior part of
297 the head or nasal region to the left. In dorsal views, the lateral part of the head is always
298 uppermost. Unless stated otherwise, the video clips and figures show the *right* side of the
299 specimens or models. Superior views are those normal to the nasal region. Copyright of the
300 images of the specimens belongs to the Natural History Museum, London, UK.

301

302 3. Results

303

304 3.1. Nasal anatomy

305 The nasal anatomy of the two specimens from which we created our models is consistent
306 with previous descriptions of the pike's nasal anatomy (Burne, 1909; Teichmann, 1954; Holl,
307 1965), and with our observations of pike *in vivo* (Section 2.2). Each of the two nasal regions
308 (Fig. 7) comprises a nasal chamber (Fig. 8, yellow outlines) linked to the external
309 environment by an incurrent nostril and an excurrent nostril (Figs. 7 and 8, IN and EN). The
310 volumes of the nasal chambers were 3 and 20 mm³ (juvenile and adult pike, respectively).
311 The ratio of the area of the incurrent nostril to that of the excurrent nostril was 1:1 in both
312 specimens. The incurrent nostril is separated from the excurrent nostril by a nasal bridge
313 (Figs. 7 and 8, NB). The dorsal edge of the nasal bridge protrudes from the surface of the
314 head (Fig. 8, asterisked sections). Internally, the incurrent nostril is connected to the
315 excurrent nostril by a single (nasal) passage (Figs. 8 and 9, NP). A radial array of low folds
316 occupies the floor of the nasal chamber (Fig. 10). We refer to this array as the olfactory
317 rosette, and to the folds as nasal folds (Figs. 8 and 10, NF). The sensory olfactory epithelium
318 resides in patches between the nasal folds, but not on the folds themselves (Fig. 1F, inset,
319 white regions; Figs. 26 and 27 of Holl, 1965). Consequently, we refer to the channels formed
320 by adjacent nasal folds as sensory channels (Figs. 7, 9 and 10, green disks). Finally, there is a
321 complementary interaction between the central posterior nasal fold (Fig. 9, yellow disks) and
322 the ventral surface of the nasal bridge (Fig. 9, asterisks).

323

324 3.2. Dye visualisation

325 Using dye visualisation, we established that flow of water through the nasal chambers of the
326 model pike could be induced by free-stream flow at Reynolds numbers of 200 – 300 (Fig.
327 11A – F; Video clips 1 – 10). In doing so, we observed that:

328

329 1) The rostrum deflected dye into the nasal region (Fig. 11B; Video clips 2 and 3). 2) Dye
330 fanned in front of the nasal region (Video clips 4 and 7). Such behaviour indicated that flow
331 was decelerating and therefore that the nasal region was a region of relatively high static
332 pressure (Shapiro, 1972). 3) Dye entered the nasal chamber via the incurrent nostril, and
333 exited via the excurrent nostril, confirming the roles of these two apertures (Fig. 11A – F). 4)
334 Within the nasal chamber, dye took either a medial or a lateral route (Fig. 11D, Me and Lt;

335 Videos clips 6 and 7). 5) Dye could circulate in the incurrent nostril in a manner suggestive of
336 a vortex (Fig. 11E, blue disk; Video clips 8 and 9; Lugt, 1983). 6) In the model of the adult
337 pike, dye appeared to pass through the posterior sensory channels (Figs. 7B, green disk, and
338 11F; Video clip 10). 7) Dye could be deflected dorsally by the nasal bridge (Fig. 11G; Video
339 clip 11). (Video clip 11 guided our choice of the vorticity value that we used to define the
340 thickness of the boundary layer; Section 2.7.3.) 8) In the model of the juvenile pike, dye
341 passed over the excurrent nostril in a manner suggestive of another vortex (Fig. 11H, blue
342 disk; Video clip 12). 9) Dye exiting the excurrent nostril passed over the lower part of the eye
343 in the juvenile pike and under the eye in the adult pike (Figs. 11A, D – F, and A.8B, asterisks,
344 Appendix A.5; Video clips 1, 4, 7, 9 and 10).

345

346 *3.3. Computational fluid dynamics*

347

348 *3.3.1. General*

349 The results from the CFD simulations were consistent with the dye visualisation experiments,
350 indicating that the CFD results were valid. For example, dye behaviour in the flume could be
351 replicated by streamlines generated from the CFD simulations (Fig. 11), including:

352

353 1) The rostral route taken by olfactory flow (Fig. 11B). 2) The two routes through the nasal
354 chamber (Fig. 11D, Me and Lt). 3) The vortex in the incurrent nostril (Fig. 11E, blue disk). 4)
355 Flow through the posterior sensory channels of the adult pike (Figs. 7B and 11F). 5)
356 Deflection of flow over the nasal bridge (Fig. 11G). 6) The vortex in the excurrent nostril of
357 the juvenile pike (Fig. 11H, blue disk).

358

359 The CFD simulations also showed that, as suggested by the dye visualisation experiments:

360

361 1) Flow decelerated in the nasal region (Fig. 12A, streamlines 1 and 2). 2) The anterior nasal
362 region was a region of relatively high static pressure ($C_p > 0$; Fig. 13).

363

364 Additionally, the CFD simulations showed that:

365

366 1) The model's stagnation point was located on the rostral tip (Fig. 13, main images, white
367 disks). 2) The anterior surface of the nasal bridge was a region of relatively high static pressure

368 (Fig. 13, insets). 3) The point of maximum pressure on the anterior surface of the nasal bridge
369 (Fig. 13, insets, white disks) was located just lateral to its midline (Fig. 13A, inset, dashed
370 yellow line). 4) This location was relatively insensitive to changes in the yaw angle (Fig. 13,
371 insets, white disks; each white disk encompasses the point of maximum static pressure for each
372 of the three different yaw angles, i.e. $0 \pm 5^\circ$). 5) 38 – 40 % of the dynamic pressure of the
373 external flow was harnessed by the nasal region in the juvenile pike, 26 – 29 % by the nasal
374 region in the adult pike. 6) The incurrent vortex, the excurrent vortex, and the two routes
375 through the nasal chamber persisted at different yaw angles ($0 \pm 5^\circ$; Fig. 12D). 7) Flow
376 decelerated as it approached the nasal chamber floor (Fig. 14B and D). 8) The anterior part of
377 the nasal chamber floor was a region of relatively high static pressure (Fig. 14A and C). 9) The
378 anterior edge of the central posterior nasal fold (Fig. 14, yellow asterisks) was a region of
379 particularly high static pressure (Fig. 14A and C, white disks). 10) Streamlines impinging on
380 the centre of the olfactory rosette dispersed over the entire rosette (Fig. 14). 11) In general,
381 these radially-dispersed streamlines passed along the sensory channels, including, as suggested
382 in Section 3.2, the posterior sensory channels (Fig. 14, e.g. yellow arrows). Some radially-
383 dispersed streamlines, however, passed *over* the nasal folds (Fig. 14, black asterisks). 12) The
384 speed along the radially-dispersed streamlines in the incurrent nostril was relatively high (Fig.
385 15). 13) The vortex in the excurrent nostril in the juvenile pike (Fig. 12C, V2) could apparently
386 entrain fluid from within the nasal chamber (Fig. 12C, blue streamlines). 14) Reynolds numbers
387 in the nasal passage were 10 (juvenile pike) and 20 (adult pike). 15) The volumetric flow rate
388 through the nasal chamber was 10 and 60 mm³ s⁻¹ (juvenile and adult pike, respectively –
389 approximately three nasal chamber volumes s⁻¹ for each model).

390

391 3.3.2. *Boundary layer*

392 We used CFD to define the boundary layer in the wild type and mutant models (Fig. 16, BL).
393 (Wild type models had intact nasal regions; the nostrils and nasal chambers of the mutant
394 models were replaced by a smooth surface; Section 2.4.) For the wild type models the
395 boundary layer (Fig. 16B and D, blue regions) was for the most part superimposable on the
396 boundary layer of the mutant models (the outer extent of which is indicated by each dashed
397 black line in Fig. 16B and D). There was, however, a bulge over the excurrent nostril in the
398 boundary layer of each wild type model (Fig. 16B and D, asterisks). The extent of the bulge
399 correlated with the extent to which the nasal bridge protruded from the surface of the head.
400 Thus the bulge was greater in the wild type model of the adult pike (Fig. 16D, asterisk). The

401 boundary layer above the dorsal edge of the nasal bridge was comparatively thinner for the
402 wild type model of the adult pike (Fig. 16D). In neither wild type model (juvenile or adult)
403 did the nasal bridge protrude from the boundary layer (Fig. 16B and D).

404

405 We also found that free-stream flow sampled by the nasal chamber entered the boundary
406 layer near the rostral tip (Fig. 16A and C, yellow regions). The time taken (t , Fig. 16A and C)
407 for a fluid particle travelling along a streamline to get from its point of entry into the
408 boundary layer to the incurrent nostril varied from 0.2 to 1.8 s in the juvenile pike and 0.3 to
409 3.1 s in the adult pike. The time taken for external flow to travel the horizontal distance from
410 the rostral tip to the centre of the incurrent nostril was 0.1 s (juvenile pike) and 0.3 s (adult
411 pike). The maximum delay caused by the boundary layer was therefore 1.7 s (juvenile pike)
412 and 2.8 s (adult pike).

413

414 3.3.3. Drag

415 We also used CFD to determine the drag incurred by the models of the pike's head, including
416 the contributions to the overall drag of pressure drag and viscous drag (Shapiro, 1961, p. 81).
417 The results were similar for both the juvenile and the adult pike (Table 1). Viscous drag was
418 the major contributor (76 – 86 %) to the total drag of each model (Table 1, grey entries),
419 suggesting that the models were streamlined (Massey, 1989, p. 255), and that the artificial tail
420 (Fig. A.4, Appendix A.5) prevented separation at the back of the head, thereby fulfilling its
421 intended function (Appendix A.1.7.1). In the mutant models, the nasal regions contributed 5.3
422 or 3.6 % (first percentage here and below: juvenile pike; second percentage: adult pike) to the
423 total drag (Table 1, yellow entries). The nasal regions of the wild type models made almost
424 the same contribution to the total drag (5.4 or 4.0 %; Table 1, gold entries) as the nasal
425 regions of the mutant models. Thus, for the wild type and mutant models derived from the
426 same specimen (e.g. the juvenile pike), the contribution of the nasal regions to the total drag
427 of the wild type model was only 0.1 or 0.4 % greater than that of the nasal region of the
428 mutant model. Viscous drag made only a small contribution (12 – 23 %; Table 1, blue
429 entries) to the total drag of the nasal regions in both the wild type and the mutant models.

430

431 **4. Discussion**

432

433 *4.1. Flow through the pike's nasal chamber is induced by an external flow*

434 We showed that flow of water through the nasal chamber of the pike can be induced by an
435 external flow at physiologically relevant Reynolds numbers (200 – 300). *In vivo*, the origin of
436 the external flow may be a water current in one of the pike's varied habitats (e.g. lake,
437 stream, or river; Masters et al., 2002) or the movement of the pike as it swims forward (e.g.
438 when moving from one habitat to another; Chapman and Mackay, 1984; Masters et al., 2002).

439

440 *4.2. Age-related differences in the pike's nasal anatomy*

441 The principal differences between the nasal anatomy of the juvenile and adult pike are: 1) the
442 nasal region of the adult pike is larger than that of the juvenile pike; 2) the dorsal edge of the
443 nasal bridge protrudes more from the surface of the adult pike's head (cf. asterisked sections,
444 Fig. 8); 3) the complementary interaction between the ventral surface of the nasal bridge and
445 the central posterior nasal fold is more marked in the juvenile pike (cf. Fig. 9A and B); and 4)
446 the nasal folds are more pronounced in the adult pike (cf. Fig. 14B and D). We discuss in the
447 ensuing sections how these differences influence both olfactory flow and odorant transport.
448 Because the differences may offset one another, we do not state whether overall they might
449 have benefitted *in vivo* one specimen more than the other.

450

451 *4.3. Key elements in the pike's olfactory flow*

452 Olfactory flow in the pike comprises four key elements (summarised in Fig. 17):

453

454 1) Flow deflected dorsally and ventrally by the nasal bridge (Fig. 12A, streamlines 1 and 2,
455 and Fig. 17, red disk and arrow).

456

457 2) Flow dispersed on the nasal chamber floor (Fig. 14, and Fig. 17, white disk).

458

459 The origins of flow elements 1) and 2) are discussed in Sections 4.4 and 4.6, respectively.

460

461 3) A vortex in the incurrent nostril ('incurrent vortex'; Figs. 12B and 17, V1; Video clips 8
462 and 9). The incurrent vortex is likely to arise when flow passing over the anterior rim of the
463 incurrent nostril separates from the surface of the head. Separation occurs because the surface
464 suddenly expands at this point (Chang, 1976, p. 3). The sudden expansion causes an adverse

465 pressure gradient, which in turn causes flow to reverse and a vortex to form (Fox, 1974, p.
466 163). A rearward-facing step, a curved wall, and a sudden enlargement in a pipe have similar
467 effects on flow (Fig. 6.16 of Fox, 1974; Fig. 1.4a of Chang, 1976; Fig. 38 of Van Dyke,
468 1982).

469

470 4) A vortex in the excurrent nostril ('excurrent vortex'; Figs. 12C and 17, V2, inset; Video
471 clip 12). The excurrent vortex is present in the olfactory flow of the juvenile pike only. It
472 occupies the medial part of the excurrent nostril (Fig. 12C, yellow streamlines). Formation of
473 the excurrent vortex is likely to arise in the same manner as the incurrent vortex, with
474 external flow separating as it passes over the medial rim of the excurrent nostril (Fig. 12C,
475 blue asterisk). A shallow cavity has a similar effect on flow (Fig. 1.4b of Chang, 1976; Fig.
476 14 of Van Dyke, 1982). The absence of an excurrent vortex in the adult pike is presumably
477 due to the more dorsally extended nasal bridge (Fig. 12A, circle), which may prevent external
478 flow passing directly over the medial part of the excurrent nostril.

479

480 All four flow elements persisted at different yaw angles ($0 \pm 5^\circ$) in the CFD simulations (e.g.
481 Fig. 12D, V1).

482

483 *4.4. Factors determining externally-induced flow through the nasal chamber*

484 Externally-induced flow through the nasal chamber may be attributed to:

485

486 1) The location of the incurrent nostril in a region of relatively high static pressure ($C_p > 0$;
487 Fig. 13). The relatively high static pressure in this region will force flow into the nasal
488 chamber.

489

490 2) The nasal bridge impeding external flow. The nasal bridge is both fully exposed to the
491 oncoming external flow (Fig. 13, insets) and normal to this flow (Fig. 8, vertical arrows).
492 Consequently, it will act like a flat plate normal to flow (Schlichting, 1960, p. 33; Fig. I.4 of
493 Thwaites, 1960; Fig. 10.4b of Douglas et al., 1985), deflecting flow a) under its ventral edge
494 and into the nasal chamber, and b) over its dorsal edge (Fig. 17, red arrow). The idea that the
495 nasal bridge deflects flow into the pike's nasal chamber was suggested by Burne (1909).

496

497 Because the nasal bridge impedes flow, it is a region of particularly high static pressure (Fig.
498 13, insets, area between dashed black lines). The point of highest pressure on the nasal bridge

499 (just lateral to its midline; Fig. 13, insets, white disks) is consistent with the direction from
500 which rostral flow approaches the nasal region (Fig. 11B). The invariance of this location
501 with yaw (Fig. 13, insets, white disks) explains why the key olfactory flow elements persist at
502 different yaw angles (Fig. 12D). This invariance also suggests that flow through the nasal
503 chamber will occur even if a stationary pike is not directly facing an oncoming water current,
504 a situation that might arise when it is waiting to ambush prey (Wheeler, 1969, pp. 166-167).

505

506 The nasal bridge's ability to impede flow is no doubt aided by the fact that it is fairly rigid.
507 Thus, the nasal bridges of the two preserved specimens resisted gentle pushing with blunt-
508 ended tweezers (the nasal bridges behaved like durable foam, returning to their original shape
509 after being pushed). Admittedly this resistance may have been due to several decades of
510 storage in preservative fluid. Any rigidity in the specimens' nasal bridges *in vivo* must have
511 stemmed from the nasal morphology, because these nasal bridges were not supported by
512 cartilage. Thus, there are in the micro-CT scans no intense pixels (indicative of cartilage) in
513 the nasal bridge regions (Fig. 2, NB). Cartilage is, however, present in the nasal bridges of
514 older specimens (Holl, 1965). We also noted that the dorsal edges of the nasal bridges of the
515 aquarium specimens were not deflected when these specimens swam forwards.

516

517 3) The excurrent nostril lying normal to the external flow (Fig. 8, vertical arrows). As a
518 result, the fluid within the excurrent nostril should experience only the ambient static pressure
519 of the external flow (Vogel, 1994, p. 60), thereby creating a positive pressure difference
520 across the nostrils. In fact, the static pressure of the fluid within the excurrent nostril was very
521 close to ambient static pressure ($C_p \sim 0 - 0.1$).

522

523 4) Viscous entrainment (Cox, 2008). Fluid may be drawn *into* the nasal chamber (Fig. 17,
524 dashed yellow circle) by the tractive viscous forces applied to it by the incurrent vortex (Fig.
525 17, V1) and by flow deflected ventrally by the nasal bridge (Fig. 17, red arrow). Fluid may be
526 drawn *out of* the nasal chamber (e.g. Fig. 17, white arrow) by the tractive viscous forces
527 applied to it by external flow passing directly over the excurrent nostril (Fig. 17, red arrow).
528 The effect of the nasal bridge, which protrudes from the surface of the head (Fig. 8,
529 asterisked sections), is to accelerate flow in this region (resulting in a thinner boundary layer
530 here than for the mutant models; Fig. 16B and D), thereby increasing these tractive viscous
531 forces. (In the mutant models, the nostrils and nasal chambers were replaced by a smooth
532 surface.) The tractive viscous forces are likely to be greater in the adult pike than in the

533 juvenile pike because the adult pike's nasal bridge protrudes dorsally to a greater extent than
534 the juvenile's (cf. asterisked sections, Fig. 8). Consequently, there will be at this point a
535 thinner boundary layer (cf. Fig. 16B and D). In the juvenile pike, fluid may also be drawn
536 from the nasal chamber (Fig. 17, yellow arrow, inset) by the excurrent vortex (Fig. 17, V2,
537 inset).

538

539 *4.5. Other mechanisms that may generate flow through the nasal chamber*

540 Two other ways in which flow through the pike's nasal chamber may be generated are: 1) by
541 the co-ordinated beating of the non-sensory cilia (Reiten et al., 2017) on the nasal folds (Fig.
542 30 of Holl, 1965); and 2) when water is drawn into the mouth during respiration. Our
543 inanimate plastic models did not allow us to investigate ciliary-driven flow, so this remains a
544 possibility in the pike. From our observations of the aquarium specimens, however, we
545 conclude that respiration is unlikely to assist flow through the pike's nasal chamber. Thus,
546 although the mouths of these specimens remained slightly open when they cruised, we could
547 see no independent movements of their jaws. When the pike were stationary, their mouths
548 were again slightly open, and there were small movements of their jaws, particularly the
549 lower jaw, but we thought these movements were not sufficient to cause flow through the
550 nasal chamber.

551

552 *4.6. Dispersal of flow over the olfactory sensory surface*

553 Flow may be dispersed over the pike's olfactory sensory surface by:

554

555 1) Impaction on the nasal chamber floor. Relatively high-speed incurrent flow (Fig. 15)
556 decelerates as it approaches the centre of the olfactory rosette, leading to radial dispersal of
557 flow over the entire nasal chamber floor, particularly in the sensory channels (Fig. 14B and
558 D). As a result of the impact, the anterior part of the nasal chamber floor is a region of
559 relatively high static pressure (Fig. 14A and C). It is probably not a coincidence that the
560 centre of the olfactory rosette (Fig. 7, black disks) is located where the relatively high-speed
561 incurrent flow strikes the nasal chamber floor. Impact-driven dispersal may be aided by the
562 radially-arranged nasal folds acting as guides to flow (Fig. 14). The nasal folds are more
563 pronounced in the adult pike (cf. Fig. 14B and D), and should therefore be better guides than
564 the nasal folds in the juvenile pike. Flow over the nasal chamber floor is not, however,
565 entirely constrained by the nasal folds: it can also pass *over* them (Fig. 14, black asterisks).

566 The dispersal of flow over the pike's olfactory rosette by impaction is reminiscent of a jet of
567 fluid spreading over a surface it strikes (Massey, 1989, p. 117).

568

569 2) The central posterior nasal fold. The central posterior nasal fold (Fig. 14, yellow asterisks)
570 splits flow in the nasal passage into a lateral stream and a medial stream (Fig. 14, yellow
571 arrows; see also Video clips 6 and 7). A region of relatively high static pressure on the
572 anterior edge of the central posterior nasal fold (Fig. 14A and C, white disks) testifies to this
573 fold's flow-splitting role. The division of flow into two streams may be assisted by the
574 complementary interaction between the central posterior nasal fold and the ventral surface of
575 the nasal bridge (Fig. 9). This interaction is particularly noticeable in the juvenile pike (cf.
576 Fig. 9A and B).

577

578 3) The incurrent vortex. The incurrent vortex directs flow a) over the *anterior* section of the
579 nasal chamber floor (opposite to the direction of the free-stream flow; Fig. 17, arrow 1) and
580 b) through the medial section of the nasal passage (Fig. 12B).

581

582 *4.7. The influence of the boundary layer on odorant transport*

583 The boundary layer may delay odorant transport from the external environment to the nasal
584 region of a fish (Denny, 1993, p. 138). The delay for the pike may be considerable (up to ~ 3
585 s). Such long delays may be (unavoidably) detrimental to its olfactory abilities. The
586 maximum delay for the adult pike is probably longer than that for the juvenile pike because
587 the rostrum of the adult pike is blunter than that of the juvenile's (cf. Fig. 1C and D,
588 arrowheads).

589

590 *4.8. The drag incurred by the nasal region*

591 The drag incurred by the nasal region of the wild type models (nasal region intact) is almost
592 the same as the drag incurred by the nasal region of the mutant models (nostrils and nasal
593 chamber replaced by a smooth surface). Thus olfactory sampling in the pike may be achieved
594 whilst incurring little additional drag (relative to the mutant head).

595

596 The relatively small contribution (~ 10 – 25 %) of viscous drag to the total drag of the nasal
597 region of the wild type models can be explained as follows. Substantial parts of the nasal
598 bridge and the nasal passage are normal to flow (Fig. 8). The viscous forces experienced by

599 flow in these regions will therefore be normal to external flow (Fig. 17, arrows 2 – 4) and
600 should therefore not contribute greatly to viscous drag. On the other hand, the viscous forces
601 associated with that part of the flow in the incurrent vortex moving in an *anterior* direction
602 (Fig. 17, V1 and arrow 1) should provide (an extremely small) *thrust*. It is noteworthy that
603 the viscous drag in the nasal region of a wild type model matches or is almost identical to that
604 of the corresponding mutant model (Table 1, blue entries) even though the surface area of the
605 nasal region of the wild type model is approximately twice that of the mutant model.

606

607 Crucially, the boundary layer in the nasal region of the wild type models remains attached to
608 the surface of the head (Fig. 16B and D). If the boundary layer separated, a wake would form,
609 leading to increased drag (Massey, 1989, p. 255). Separation of the boundary layer can only
610 occur in the presence of *both* an adverse pressure gradient *and* adverse viscous forces
611 (Chang, 1970, p. 5). The boundary layer *cannot* separate if one of these influences is absent.
612 Separation of the boundary layer in the nasal region of the pike is avoided because:

613

614 1) Flow accelerates over the dorsal edge of the nasal bridge, as evidenced by the thin
615 boundary layer and condensed isotachs (lines of equal flow speed; Vogel, 1994, p. 45) in this
616 region (Fig. 16B and D, round insets). In other words, there is a favourable pressure gradient
617 here, and therefore the boundary layer cannot separate.

618

619 2) Flow striking the nasal bridge experiences an adverse pressure gradient but *not* adverse
620 viscous forces. Adverse viscous forces are reduced because the viscous forces associated with
621 flow that has been deflected dorsally and ventrally over the surface of the nasal bridge are
622 largely *normal* to the external flow (Fig. 17, arrows 2 and 3). In the absence of substantial
623 adverse viscous forces, the boundary layer cannot separate.

624

625 3) The nasal bridge may be streamlined (Kaufmann, 1974, pp. 6-7). The nasal bridge is
626 tapered in sagittal cross-section, with a rounded ventral edge and a thinner, but still rounded,
627 dorsal section (Fig. 8), not unlike an aerofoil (Fig. 10.16 of Douglas et al., 1985). Indeed,
628 flow in the vicinity of the nasal bridge's dorsal edge behaves like flow passing over the
629 trailing edge of an aerofoil. For example, streamlines deflected dorsally and ventrally by the
630 nasal bridge meet and depart smoothly from its dorsal edge (Figs. 12A, asterisk, and 17, red
631 arrow). They do not form a wake (cf. Fig. 10c of Goldstein, 1965).

632

633 4) Separated flow is controlled. Flow becomes separated from the surface of the head at two
634 locations in the nasal region. One location is the dorsal edge of the nasal bridge (Fig. 17, red
635 arrow). As described in 3) above, no wake is formed here. The other location is the rim of the
636 incurrent nostril (Fig. 17, IN). Part of this separated flow forms the incurrent vortex (Fig. 17,
637 V1). Although a vortex could potentially form a wake (Fig. 10.26 of Douglas et al., 1985), it
638 does not do so here because it is effectively destroyed when it passes through the nasal
639 passage (Fig. 12B). The other part of the flow that separates from the rim of the incurrent
640 nostril becomes reattached either to the nasal bridge (Fig. 17, red disk) or to the nasal
641 chamber floor (Fig. 17, white disk), or it passes through the nasal chamber (Fig. 17, yellow
642 arrow). Reattachment to the nasal chamber floor serves to trap partly the incurrent vortex as a
643 separation bubble (Fig. 37 of Chang, 1970). Reattachment of flow to the nasal bridge may be
644 aided by the relatively narrow spacing between the nasal bridge and the rim of the incurrent
645 nostril (Panton, 1984, p. 541). Thus, although flow *does* separate from the surface of the head
646 in the nasal region, it does *not* lead to the separation of the boundary layer.

647

648 Evidence that the boundary layer remains attached to the nasal region of the pike *in vivo*
649 came from an observation of one of the aquarium specimens. This specimen had a fine thread
650 attached to its left nasal bridge. When the specimen swam, the thread trailed without
651 wavering. (A wavering thread would have indicated separation.)

652

653 4.9. Other aspects of olfactory flow

654 Reynolds numbers in the nasal chamber are low (10 – 20). Viscous forces here are, therefore,
655 relatively large (Shapiro, 1961, p. 78). The viscous nature of flow in the nasal chamber is
656 evident from the absence of separation when flow passes over, rather than along, the nasal
657 folds (Fig. 14, black asterisks). The floor of the nasal chamber may therefore be considered
658 hydrodynamically smooth (Shapiro, 1961, p. 121), despite the presence of the nasal folds.

659

660 The incurrent vortex may encourage odorant transport to the olfactory sensory surface by
661 bringing several times the same fluid particle into proximity with the surface (Fig. 12B, inset,
662 blue disks). Thus, the incurrent vortex may allow the fluid to be resampled by the olfactory
663 sensory surface. Olfactory resampling may also occur in the European eel (*Anguilla anguilla*;
664 Teichmann, 1959).

665

666 4.10. Comparison with externally-induced olfactory flow in the sturgeon

667 Externally-induced olfactory flow in the pike is similar in several ways to that in the
668 sturgeon, *Huso dauricus* (Garwood et al., 2019):

669

670 1) Both the pike and the sturgeon have an incurrent nostril located in a region of relatively
671 high static pressure, where flow will be forced into the nasal chamber.

672

673 2) Both fishes have a feature that impedes external flow, deflecting it into the nasal chamber.
674 In the sturgeon this feature is the lateral wall of the incurrent nostril. In the pike, it is the nasal
675 bridge.

676

677 3) Both fishes have an excurrent nostril normal to external flow. Consequently, in both fishes
678 the fluid in the excurrent nostril experiences a static pressure equal or close to the ambient
679 static pressure of the external flow.

680

681 4) In both the pike and the sturgeon, flow is dispersed over the olfactory sensory surface by a
682 jet impingement-like mechanism. Specifically, dispersal occurs when relatively high speed
683 incurrent flow decelerates on encountering an internal nasal surface (the central support in the
684 sturgeon; the nasal chamber floor in the pike).

685

686 5) Vortices may assist olfaction in both fishes. Vortices in the nasal chamber of the sturgeon,
687 like those in the pike, may assist flow through the nasal chamber by viscous entrainment.

688

689 Furthermore, the percentage of the dynamic pressure of the free-stream flow harnessed by the
690 nasal regions of both fishes is similar (pike: ~ 25 – 40 %; sturgeon: ~ 35 %). The dye
691 visualisation experiments suggested, however, that the sturgeon's nasal region is better at
692 harnessing external flow than the pike's. Thus, in the dye visualisation experiments with the
693 sturgeon model, the dye filament passed largely intact into the incurrent nostril (e.g. Video
694 clip 1 of Garwood et al., 2019). With the pike models, however, not all the dye impinging on
695 the incurrent nostril passed into it (e.g. Video clip 2). Furthermore, in the CFD simulations of
696 olfactory flow in the juvenile pike, a streamline that impacted on the nasal chamber floor
697 could subsequently pass *out* of the incurrent nostril (Fig. 14A and B, black arrows).

698

699 The sturgeon's nasal region may appear to be better at harnessing external flow than the
700 pike's because the fluid dynamics experiments with the sturgeon models were performed at
701 higher Reynolds numbers than those with the pike models (500 v. 200 – 300, respectively).
702 We note also that the sturgeon's excurrent nostril is in a region of low static pressure ($C_p <$
703 0), where there will be a tendency for flow to be drawn out of it. The pike's excurrent nostril,
704 on the other hand, is essentially in a region where $C_p > 0$ (Fig. 13). In addition, the sturgeon's
705 excurrent nostril is three times larger than its incurrent nostril, whereas the pike's excurrent
706 nostril is about the same size as its incurrent nostril. Viscous entrainment of flow from the
707 sturgeon's excurrent nostril may therefore be more effective than from the pike's (Vogel,
708 1978).

709

710 *4.11. Limitations*

711 Many of the limitations of the current study (and, where possible, their mitigation) are
712 common to our previous studies (Abel et al., 2010; Agbesi et al., 2016a, 2016b; Garwood et
713 al., 2019), and are discussed therein (see also Appendix A.3). One limitation of note in the
714 current study was the lack of convexity in the eyes of the models of the juvenile pike (Fig.
715 3A). *In vivo*, as we observed in the aquarium and survey specimens, the eyes of the pike are
716 convex. In the preserved specimens on which our models are based, only the adult pike had
717 convex eyes. The eyes of the preserved specimen of the juvenile pike had collapsed to a
718 flattened state. We were, therefore, able only to capture the convexity of the pike's eyes in
719 the models of the adult pike specimen (Fig. 3B). We found, however, that this convexity had
720 only a minor effect on olfactory flow. Thus, in the models of the adult pike, flow passed
721 under the eye (Fig. 11, asterisks; e.g. Video clip 1), whereas in the models of the juvenile
722 pike, flow typically passed over the ventral part of the eye, not under it (Fig. A.8B, asterisk,
723 Appendix A.5; Video clip 4). But, except for the excurrent vortex in the juvenile pike, the key
724 olfactory flow elements in the models of the juvenile and adult pike were similar (cf. Video
725 clips 8 and 9, for example).

726

727 The other limitation of note in the current study was our failure to include in our models the
728 transverse nasal folds of the pike's olfactory rosette (Fig. 1F, inset, yellow disk; see also Fig.
729 27 of Holl, 1965). We were able to see (e.g. with a stereomicroscope) the transverse nasal
730 folds of the preserved specimens of the juvenile and adult pike (they gave the olfactory
731 rosette a cribriform appearance; Fig. 1F), but the micro-CT scan of each head did not resolve
732 them. (This inability was not due to the quality of the scans: the voxel size of each scan was

733 limited by the size of the head.) Nevertheless, given that the floor of the nasal region may be
734 considered hydrodynamically smooth (Section 4.9), we believe that inclusion of the
735 transverse nasal folds would not have significantly affected the key olfactory flow elements.
736

737 **5. Conclusion**

738 The nasal bridge and a vortex in the incurrent nostril play multiple roles in olfactory flow in
739 the pike, with several probable benefits for olfaction. Both features may facilitate odorant
740 transport by a) encouraging flow through the nasal chamber and b) dispersing flow over the
741 olfactory sensory surface. At the same time, drag (and therefore the metabolic cost to the
742 fish) is minimised. The nasal bridge encourages flow through the nasal chamber by
743 obstructing (via its anterior surface) and accelerating (via its dorsal edge) local external flow.
744 In addition, the nasal bridge may encourage dispersal of flow over the olfactory sensory
745 surface by diverting it (via a complementary interaction between its ventral surface and the
746 central posterior nasal fold) medially and laterally within the nasal chamber. The nasal bridge
747 minimises drag by its orthogonality to external flow, by its streamlined shape, and by
748 accelerating (again via its dorsal edge) local external flow. The incurrent vortex, which arises
749 as a result of the *provoked* separation of local external flow (via the sudden expansion of the
750 surface of the head), may encourage flow into the nasal chamber by viscous entrainment.
751 Fluid motion within the incurrent vortex encourages dispersal of flow over the anterior
752 olfactory sensory surface, which at the same time may contribute to (a small) thrust, thereby
753 minimising drag. The incurrent vortex may also encourage odorant transport to the olfactory
754 sensory surface by bringing several times the same fluid particle into contact with that
755 surface. In short, the pike's apparently simple nasal anatomy belies a remarkable piece of
756 natural engineering.
757

758 **Acknowledgements**

759 We thank: Laser Lines/Ogle Models and Prototypes for 3D printing; Brecht Morris
760 (Environment Agency, UK) and Robert Britton (University of Bournemouth, UK) for
761 allowing JPLC to observe the pike they caught during a joint Environment
762 Agency/University of Bournemouth survey; the staff of the Aquarium of the Lakes, Cumbria,
763 UK, for facilitating our other observations of pike *in vivo*; Celia Butler, Matt Cross, Paul
764 Frith, Graham Martin, and Simon Wharf for technical assistance; Ismet Gursul and Richie
765 Gill for allowing us to use, respectively, the flume and the ScanIP software in the Department
766 of Mechanical Engineering at Bath; Kevin Webb and Harry Taylor for photography; David
767 Cleaver, Oliver Crimmen, and Jos Darling for helpful discussions; Mawuli Agbesi and Flo
768 Lendrum for contributing to the initial fluid dynamics experiments on the models of the
769 juvenile pike; Xavier Mear for German to English translation, and Asel Sartbaeva for Russian
770 to English translation.

771

772 **Funding statement**

773 This work was supported by the University of Bath's Alumni Fund. The Engineering and
774 Physical Sciences Research Council, UK, funded the Henry Moseley X-ray Imaging Facility
775 through the Royce Institute for Advanced Materials (grants EP/F007906/1, EP/F001452/1,
776 EP/I02249X, EP/M010619/1, EP/F028431/1, EP/M022498/1 and EP/R00661X/1). The
777 funding sources were not involved in the conduct of the research, or the preparation of the
778 article.

779

780 **References**

- 781 Abel, R.L., Maclaine, J.S., Cotton, R., Xuan, V.B., Nickels, T.B., Clark, T.H., Wang, Z.,
782 Cox, J.P.L., 2010. Functional morphology of the nasal region of a hammerhead shark. *Comp.*
783 *Biochem. Physiol. A* 155, 464-475.
- 784 Abernathy, F.H., 1972. Fundamentals of boundary layers. In: National Committee for Fluid
785 Mechanics Films. *Illustrated Experiments in Fluid Mechanics*. MIT Press, London, pp. 75-81.
- 786 Agbesi, M.P.K., Naylor, S., Perkins, E., Borsuk, H.S., Sykes, D., Maclaine, J.S., Wang, Z.,
787 Cox, J.P.L., 2016a. Complex flow in the nasal region of guitarfishes. *Comp. Biochem.*
788 *Physiol. A* 193, 52-63.
- 789 Agbesi, M.P.K., Borsuk, H.S., Hunt, J.N., Maclaine, J.S., Abel, R.L., Sykes, D., Ramsey
790 A.T., Wang, Z., Cox, J.P.L., 2016b. Motion-driven flow in an unusual piscine nasal region.
791 *Zoology* 119, 500-510.
- 792 Ayachit, U., 2016. *The ParaView Guide*. Kitware Inc.
- 793 Barnard, R.H., Philpott, D.R., 2004. *Aircraft Flight*. 3rd ed. Pearson Education, Harlow.
- 794 Barnard, R.H., 2009. *Road Vehicle Aerodynamic Design*. 3rd ed. MechAero Publishing, St
795 Albans.
- 796 Burne, R.H., 1909. The anatomy of the olfactory organ of teleostean fishes. *Proc. Zool. Soc.*
797 *Lond.* 2, 610-663.
- 798 Chang, P.K., 1970. *Separation of Flow*. Pergamon Press, Oxford.
- 799 Chang, P.K., 1976. *Control of Flow Separation*. Hemisphere, Washington.
- 800 Chapman, C.A., Mackay, W.C., 1984. Versatility in habitat use by a top aquatic predator,
801 *Esox lucius* L. *J. Fish Biol.* 25, 109-115.
- 802 Cox, J.P.L., 2008. Hydrodynamic aspects of fish olfaction. *J. Roy. Soc. Interface* 5, 575-593.
- 803 Craig, J.F., 1996. *Pike*. Chapman & Hall, London.
- 804 Craig, J.F., 2008. A short review of pike ecology. *Hydrobiologia* 601, 5-16.
- 805 Denny, M.W., 1993. *Air and Water*. Princeton University Press, Princeton.
- 806 Devitsina, G.V., Malyukina, G.A., 1977. The functional organisation of the olfactory organ in
807 macrosomatic and microsomatic fishes. *Ichthyol. Questions* 17, 493-502. In Russian.
- 808 Douglas, J.F., Gasiorek, J.M., Swaffield, J.A., 1985. *Fluid Mechanics*. 2nd ed. Pitman,
809 Massachusetts.
- 810 Fox, J.A., 1974. *An Introduction to Engineering Fluid Mechanics*. Macmillan, London.
- 811 Fox, R.W., McDonald, A.T., Pritchard, P.J., Leylegian, J.C., 2012. *Fluid Mechanics*. 8th ed.
812 John Wiley & Sons, Asia.

813 Garwood, R.J., Behnsen, J., Haysom, H.K., Hunt, J.N., Dalby, L.J., Quilter, S.K., Maclaine,
814 J.S., Cox, J.P.L., 2019. Olfactory flow in the sturgeon is externally driven. *Comp. Biochem.*
815 *Physiol. A* 235, 211-225.

816 Garwood, R.J., Behnsen, J., Maclaine, J.S., Cox, J.P.L., 2020a. TIFF images from X-ray scan
817 of head of *Esox lucius* (adult). Mendeley Data, v1. <http://dx.doi.org/10.17632/bgv6gs9dvr.1>.

818 Goldstein, S., 1965. *Modern Developments in Fluid Dynamics*. Dover Publications, New
819 York.

820 Haynes, W.M., Lide, D.R., 2011. *CRC Handbook of Chemistry and Physics*. 92nd ed. CRC
821 Press, Boca Raton.

822 Haysom, H.K., Quilter, S.K., Dalby, L.J., Cox, J.P.L., 2019. STL models of heads of *Esox*
823 *lucius*. Mendeley Data, v1. <http://dx.doi.org/10.17632/hv4xjnznrf.1>.

824 Helfman, G.S., Collette, B.B., Facey, D.E., Bowen, B.W., 2009. *The Diversity of Fishes*. 2nd
825 ed. Wiley-Blackwell, Chichester.

826 Holl, A., 1965. Vergleichende Morphologische und Histologische Untersuchungen am
827 Geruchsorgan der Knochenfische (Comparative morphological and histological
828 investigations on the olfactory organ of bony fishes). *Z. Morph. Ökol. Tiere* 54, 707-782. In
829 German.

830 Holmes, W.M., Cotton, R., Xuan, V.B., Rygg, A.D., Craven, B.A., Abel, R.L., Slack, R.,
831 Cox, J.P.L., 2011. Three-dimensional structure of the nasal passageway of a hagfish and its
832 implications for olfaction. *Anat. Rec.* 294, 1045-1056.

833 Howard, L.E., Holmes, W.M., Ferrando, S., Maclaine, J.S., Kelsh, R.N., Ramsey, A., Abel,
834 R.L., Cox, J.P.L., 2013. Functional nasal morphology of chimaerid fishes. *J. Morph.* 274,
835 987-1009.

836 Kaufmann, J., 1974. *Streamlined*. Thomas Y. Crowell Company, New York.

837 Kline, S.J., 1972. Flow visualization. In: *National Committee for Fluid Mechanics Films.*
838 *Illustrated Experiments in Fluid Mechanics*. MIT Press, London, pp. 34-38.

839 Lugt, H.J., 1983. *Vortex Flow in Nature and Technology*. John Wiley & Sons, New York.

840 Massey, B.S., 1989. *Mechanics of Fluids*. 6th ed. Van Nostrand Reinhold, London.

841 Masters, J.E.G., Welton, J.S., Beaumont, W.R.C., Hodder, K.H., Pinder, A.C., Gozlan, R.E.,
842 Ladle, M., 2002. Habitat utilisation by pike *Esox lucius* L. during winter floods in a southern
843 English chalk river. *Hydrobiologia* 483, 185-191.

844 Nelson, J.S., 2006. *Fishes of the World*. 4th ed. John Wiley & Sons, New Jersey.

845 Panton, R.L., 1984. *Incompressible Flow*. John Wiley & Sons, New York.

846 Raat, A.J.P., 1988. Synopsis of Biological Data on the Northern Pike, *Esox lucius* Linnaeus,
847 1758. FAO Fisheries Synopsis No. 30 Rev. 2. Food and Agriculture Organization of the
848 United Nations, Rome.

849 Ramsey, A., Houston, T.F., Ball, A.D., Goral, T., Barclay, M.V.L., Cox, J.P.L., 2015.
850 Towards an understanding of molecule capture by the antennae of male beetles belonging to
851 the genus *Rhipicera* (Coleoptera, Rhipiceridae). *Anat. Rec.* 298, 1519-1534.

852 Ramsey, A.T., Maclaine, J.S., Cox, J.P.L., 2020. TIFF images from X-ray scan of head of
853 *Esox lucius* (juvenile). Mendeley Data, v1. <http://dx.doi.org/10.17632/g5vx38jh5j.1>.

854 Reiten, I., Uslu, F.E., Fore, S., Pelgrims, R., Ringers, C., Verdugo, C.D., Hoffman, M., Lal,
855 P., Kawakami, K., Pekkan, K., Yaksi, E., Jurisch-Yaksi, N., 2017. Motile-cilia-mediated flow
856 improves sensitivity and temporal resolution of olfactory computations. *Curr. Biol.* 27, 166-
857 174.

858 Schlichting, H. 1960. *Boundary Layer Theory*. McGraw-Hill, New York.

859 Shapiro, A.H., 1961. *Shape and Flow*. Heinemann, London.

860 Shapiro, A.H., 1972. Pressure fields and fluid acceleration. In: National Committee for Fluid
861 Mechanics Films, *Illustrated Experiments in Fluid Mechanics*. MIT Press, London, pp. 39-46.

862 Teichmann, H., 1954. Vergleichende Untersuchungen an der Nase der Fische (Comparative
863 studies on the nose of the fish). *Z. Morph. Ökol. Tiere* 43, 171-212. In German.

864 Teichmann, H., 1959. Über die Leistung des Geruchssinnes beim Aal [*Anguilla anguilla* (L.)]
865 (On the performance of the sense of smell of the eel). *Z. vgl. Physiol.* 42, 206-254. In German.

866 Theisen, B., 1982. Functional morphology of the olfactory organ in *Spinachia spinachia* (L.)
867 (Teleostei, Gasterosteidae). *Acta Zool.* 63, 247-254.

868 Thwaites, B., 1960. *Incompressible Aerodynamics*. Clarendon Press, Oxford.

869 Van Dyke, M., 1982. *An Album of Fluid Motion*. The Parabolic Press, Stanford.

870 Vogel, S., 1978. Organisms that capture currents. *Sci. Am.* August, 108-117.

871 Vogel, S., 1988. How organisms use flow-induced pressures. *Am. Sci.* 76, 28-34.

872 Vogel, S., 1994. *Life in Moving Fluids*. 2nd ed. Princeton University Press, Princeton.

873 Wang, Z.-J., Jiang, P., Gursul, I., 2007. Effect of thrust-vectoring jets on delta wing
874 aerodynamics. *J. Aircraft* 44, 1877-1888.

875 Webb, P.W., 1984. Form and function in fish swimming. *Sci. Am.* July, 72-82.

876 Weller, H.G., Tabor, G., Jasak, H., Fureby, C., 1998. A tensorial approach to computational
877 continuum mechanics using object-oriented techniques. *Comp. Phys.* 12, 620-631.

878 Wheeler, A., 1969. *The Fishes of the British Isles and North-West Europe*. Macmillan,
879 London.

880 Zeiske, E., Theisen, B., Breucker, H., 1992. Structure, development, and evolutionary aspects
881 of the peripheral olfactory system. In: Hara, T.J. (Ed.), Fish Chemoreception. Chapman &
882 Hall, London.
883

884 **Figure legends**

885

886 **Fig. 1** The two pike (*Esox lucius*) specimens used to generate the fluid dynamics models. (A),
887 (C) and (E): Juvenile pike (BMNH 1963.4.26.2). (B), (D) and (F): Adult pike (BMNH
888 1986.5.20.4). (A) and (B): Complete specimens; (C) and (D): heads; (E) and (F): superior
889 view of each nasal region. Inset in (D): magnified nasal region. Inset in (F): magnified yellow
890 highlighted section, main image. White regions in inset (F): location of sensory olfactory
891 epithelium. Yellow disk in inset (F): transverse fold. Specimen in (B) and (D) outlined in
892 white to improve contrast with background. Nostrils filled in black in (C), for emphasis.
893 Arrowheads in (C) and (D): anterior rostral edge. White marks, panel frames (A) – (D):
894 posterior extent of X-ray scan (A and B); location of TIFF images shown in Fig. 2 (C and D).
895 Yellow marks in (D): location of TIFF image, Fig. A1.C, Appendix A.5. a: Anterior; AF:
896 anal fin; EN: excurrent nostril; *FL*: fork length (distance from rostral tip to asterisk); IN:
897 incurrent nostril; l: lateral; m: medial; NB: nasal bridge (extent indicated by dashed black
898 lines); NR: nasal region; p: posterior; PF: pectoral fin; Ro: rostrum.

899

900 **Fig. 2** TIFF images from micro-CT scans of (A) juvenile and (B) adult pike. Transverse
901 cross-section through each head (location indicated in Fig. 1C and D, respectively). Yellow
902 line: perimeter of nasal chamber. Ai: Air; Bo: bone; d: dorsal; NB: nasal bridge; OC: oral
903 cavity; Ti: tissue; v: ventral.

904

905 **Fig. 3** Surface models of heads of (A) juvenile and (B) adult pike. Insets: magnified nasal
906 region. Dashed lines in insets: limits of nasal bridge. Positive and negative yaw angles
907 indicated by red and blue arrows, respectively. EN: Excurrent nostril; Ey: eye; IN: incurrent
908 nostril; NR: nasal region.

909

910 **Fig. 4** Plastic models of heads of (A) juvenile and (B) adult pike. Insets: magnified nasal
911 region. Black lines in insets: extent of nasal chamber. EN: Excurrent nostril; Ey: eye; IN:
912 incurrent nostril; NR: nasal region; Op: opaque part; PF: pectoral fin; Tr: translucent part.

913

914 **Fig. 5** CFD mesh of adult pike. (A) Refinement of mesh on model surface, nasal region
915 (superior view). Large circles: magnified border (small circles) at two stages of refinement,
916 with refinement increasing bottom to top. (B) Transverse cross-section through mesh (same

917 cross-section as in Fig. 2B). (C) Transverse cross-section through nasal passage. Inset in (C):
918 mesh next to olfactory sensory surface (asterisked box, main image). The seams (e.g. Se) in
919 (C) are artifacts arising from the way ParaView's Slice filter cuts a mesh. Scale bars in (A)
920 and (B) and labels in all images deliberately omitted to allow reader to see mesh. a: Anterior;
921 d: dorsal; l: lateral; m: medial; p: posterior; Se: seam; v: ventral.

922

923 **Fig. 6** Characteristic dimension of adult pike's nasal region. (A) Head of surface model, right
924 half, dorsal aspect. (B) Highlighted nasal region in (A), dorsal aspect. Arrow: direction of
925 free-stream flow. a: Anterior; EN: excurrent nostril; IN: incurrent nostril; *L*: characteristic
926 dimension of nasal region; l: lateral; m: medial; NR: nasal region; p: posterior.

927

928 **Fig. 7** Detail of surface models of (A) juvenile and (B) adult pike. Superior views of nasal
929 region. Arrow: direction of free-stream flow. Asterisk: central posterior nasal fold. Black
930 disk: centre of olfactory rosette. Green disk: sensory channel. Yellow marks, panel frames:
931 positions of sagittal sections in Figs. 8, 16B, D, and 17. Black marks, panel frames: position
932 of transverse sections in Fig. 9. a: Anterior; EN: excurrent nostril; IN: incurrent nostril; l:
933 lateral; m: medial; NB: nasal bridge (extent indicated by dashed lines); p: posterior.

934

935 **Fig. 8** Detail of surface models of (A) juvenile and (B) adult pike. Sagittal sections (locations
936 indicated in Fig. 7) through nasal region (A: lateral part; B: medial part). Horizontal arrow:
937 direction of free-stream flow. Vertical arrow indicates excurrent nostril normal to flow.
938 Yellow outlines: nasal chamber. Dashed lines: rims of incurrent and excurrent nostrils. Light
939 blue asterisked section: protruding dorsal edge of nasal bridge. Black marks, panel frames:
940 position of transverse sections in Fig. 9. a: Anterior; d: dorsal; EN: excurrent nostril; IN:
941 incurrent nostril; NB: nasal bridge; NF: nasal fold; NP: nasal passage; p: posterior; v: ventral.

942

943 **Fig. 9** Detail of surface models of (A) juvenile and (B) adult pike. Transverse sections
944 through nasal passage. Location of sections given in Figs. 7 and 8. Orientations same as Fig.
945 A.5C, Appendix A.5 (juvenile pike) and Fig. 5C (adult pike). Asterisk: ventral surface of
946 nasal bridge. Yellow disk: central posterior nasal fold. Green disk: sensory channel. NB:
947 Nasal bridge; NP: nasal passage.

948

949 **Fig. 10** Detail of surface models of (A) juvenile and (B) adult pike. Olfactory rosettes (dorsal
950 sections through nasal region). Asterisk: central posterior nasal fold. Green disk: sensory
951 channel. a: Anterior; EN and IN: location of excurrent and incurrent nostrils, respectively; l:
952 lateral; m: medial; NF: nasal fold; p: posterior.

953

954 **Fig. 11** Correspondence of CFD-generated streamlines to dye behaviour in the plastic models
955 of the pike. The plastic models are represented by surface models. Streamline(s) (yellow
956 tubes) correspond to dye behaviour in: (A) Video clip 1; (B) Video clip 2; (C) Video clip 5;
957 (D) Video clip 7; (E) Video clip 9; (F) Video clip 10; (G) Video clip 11; and (H) Video clip
958 12 (video clip identified by number in box in each panel). (A) – (G): Adult pike; (H): juvenile
959 pike. (A), (D) and (H): Lateral aspect of models. (B) and (C): Dorsal aspect. (E) and (F):
960 Superior view (*left* nasal region in F). (G): Lateroventral aspect. Insets: magnified nasal
961 region. Model in (C), (D) and (E) at 50 % opacity, to match translucent right nasal region of
962 plastic model. Scale bars refer to the size of the *plastic* models. Arrow: direction of free-
963 stream flow. Black lines: extent of nasal chamber. Red disk: nasal bridge. Blue disk: vortex.
964 Asterisk: flow under eye. EN: Excurrent nostril (black on white lines); Ey: eye; IN: incurrent
965 nostril (white lines); Lt and Me: lateral and medial routes through nasal chamber,
966 respectively.

967

968 **Fig. 12** CFD-generated streamlines (tubes) in the nasal region of the pike CFD models. (A)
969 Flow deflected (1) dorsally and (2) ventrally by the nasal bridge. Adult pike, anterolateral
970 aspect. Streamlines colour-coded according to speed (U). Asterisk indicates where dorsally
971 directed flow meets ventrally directed flow. Circle: medial edge of nasal bridge. (B) Vortex
972 (V1) in incurrent nostril. Juvenile pike, superior view. Inset: side view of V1 (indicated by
973 eye in main panel), different streamline. Blue disks: points at which fluid particle in V1 is
974 near olfactory sensory surface. (C) Vortex (V2) in excurrent nostril. Juvenile pike, superior
975 view. Blue streamlines: flow passing through nasal chamber. Yellow streamlines: external
976 flow. Blue asterisk: point at which external flow passes over excurrent nostril. For (B) and
977 (C): model at 50 % opacity; black lines: limits of nasal chamber. Scale bar in (B) also applies
978 to (C). (D) Persistence of incurrent vortex at different yaw angles. Adult pike, superior view.
979 Yellow, red and blue streamlines: yaw 0° , $+5^\circ$ and -5° , respectively. Arrow: direction of
980 free-stream flow. a: Anterior; EN: excurrent nostril; IN: incurrent nostril; l: lateral; m:

981 medial; NB: nasal bridge (extent indicated by dashed lines); NC: nasal chamber; p: posterior;
982 V1: incurrent vortex; V2: excurrent vortex.

983

984 **Fig. 13** Static pressure on the surface of (A) juvenile and (B) adult pike CFD models.

985 Surfaces colour-coded according to pressure coefficient (C_p). Insets: anterior aspect of nasal
986 region. Cross (insets) and arrow (main images): direction of free-stream flow (into page for
987 cross). White lines, main images: division between $C_p > 0$ (predominantly red) and $C_p < 0$
988 (predominantly blue). Dashed black lines, insets: limits of nasal bridge. Dashed yellow line,
989 inset in (A): midline of nasal bridge. White disk (main images): stagnation points. White disk
990 (insets): region of maximum pressure in the nasal region (yaw $0 \pm 5^\circ$). d: Dorsal; EN:
991 excurrent nostril; Ey; eye; IN: incurrent nostril; l: lateral; m: medial; Ro: rostrum; v: ventral.

992

993 **Fig. 14** CFD-generated streamlines passing through olfactory sensory channels of juvenile (A
994 and B) and adult (C and D) pike CFD models. (A) and (C): Static pressure on nasal chamber
995 floor. Surface colour-coded according to pressure coefficient (C_p). (B) and (D): Flow
996 decelerating as it approaches nasal chamber floor. Streamlines colour-coded according to
997 speed (U). White arrow: flow through sensory channel. Pair of yellow arrows: flow split by
998 central posterior nasal fold (yellow asterisk). Black arrow: streamline exiting incurrent
999 nostril. White disk: point of maximum C_p on nasal chamber floor. Green disk: sensory
1000 channel. Black asterisk: streamline passing *over* nasal fold. a: Anterior; EN and IN: location
1001 of excurrent and incurrent nostrils, respectively; l: lateral; m: medial; NF: nasal fold; p:
1002 posterior.

1003

1004 **Fig. 15** Incurrent nostril entry points for CFD-generated streamlines passing through the
1005 olfactory sensory channels in the nasal chamber of (A) juvenile and (B) adult pike CFD
1006 models. Slice (grey) through CFD mesh of right incurrent nostril. Numbered black lines:
1007 speed contours normalised to maximum flow speed in slice (4.7 cm s^{-1}). 1: 0.2; 2: 0.4; 3: 0.6;
1008 4: 0.8. White region: area through which 'sensory channel' streamlines pass. a: Anterior; l:
1009 lateral; m: medial; p: posterior.

1010

1011 **Fig. 16** Boundary layers (blue) in the pike CFD models. (A) and (C): Lateral aspect of head
1012 of juvenile and adult pike, respectively. Yellow regions: space occupied by streamlines
1013 (Appendix A.1.7.5). t : time taken for a fluid particle to get from the point of entry into the

1014 boundary layer to the incurrent nostril. Insets: dorsal aspect of rostral tip (right section),
1015 showing where streamlines enter boundary layer. (B) and (D): Sagittal sections (indicated in
1016 Fig. 7) of nasal region of juvenile and adult pike, respectively. Dashed black line: outer limit
1017 of boundary layer of mutant model (Section 2.4). Dashed white line: outline of head of
1018 mutant model. Asterisk: bulge in boundary layer. Curved line: lower limit of round inset.
1019 Round inset in (B) and (D): magnified dorsal edge of nasal bridge. White lines in round inset:
1020 speed contours (normalised to maximum flow speed in corresponding slice through CFD
1021 mesh). Rectangular inset in (B): key parts of nasal region. Arrow: direction of free-stream
1022 flow. a: Anterior; BL: boundary layer; d: dorsal; EN: excurrent nostril; Ey: eye; IN: incurrent
1023 nostril; NB: nasal bridge; p: posterior; v: ventral.

1024

1025 **Fig. 17** Schematic of flow in the nasal region of the pike. Main image: sagittal section
1026 through nasal region of adult pike (location of section indicated in Fig. 7B). Inset: sagittal
1027 section through excurrent nostril of juvenile pike. Large white arrow: direction of free-stream
1028 flow. Red arrow: flow deflected dorsally and ventrally by nasal bridge. Blue arrows: vortices.
1029 Yellow arrows: central nasal passage flow. Small white arrow: sensory channel flow. Arrows
1030 1 – 4: viscous forces. Red disk: flow deflected dorsally and ventrally by nasal bridge. White
1031 disk: flow dispersed on nasal chamber floor. Dashed yellow circle: entrained fluid. a:
1032 Anterior; d: dorsal; EN: excurrent nostril; IN: rim of incurrent nostril; NB: nasal bridge; p:
1033 posterior; v: ventral; V1: incurrent vortex; V2: excurrent vortex.

1034

1035 **Video**

1036 Dye visualisation with the plastic models of the pike. Flow is left to right and the free-stream
1037 speed is 5 cm s^{-1} . Pitch and yaw are 0° . Roll angles and camera positions (Fig. A.3, Appendix
1038 A.5) are given below. Unless stated otherwise: the right nasal region is shown; the dorsal aspect
1039 camera position (Fig. A.3B, Appendix A.5) is X; and each clip is flipped horizontally.

1040

1041 **Clip 1** Adult pike. Passage of dye over rostrum and through nasal chamber. Lateral aspect of
1042 head. Roll 0° ; camera position a. Compare with Fig. 11A.

1043 **Clip 2** Adult pike. Passage of dye over rostrum and through nasal chamber. Dorsal aspect of
1044 head. Roll $+90^\circ$; camera position b. Clip rotated 180° . Compare with Fig. 11B.

1045 **Clip 3** Adult pike. Passage of dye through *left* nasal chamber. Dorsal aspect. Roll $+90^\circ$;
1046 camera position a. Compare with Fig. A.8A, Appendix A.5.

1047 **Clip 4** Juvenile pike. Passage of dye through nasal chamber. Lateral aspect. Roll 0° ; camera
1048 positions a and Y. Compare with Fig. A.8B, Appendix A.5.

1049 **Clip 5** Adult pike. Passage of dye through nasal chamber. Dorsal aspect. Roll $+90^\circ$; camera
1050 position b. Clip rotated 180° . Compare with Fig. 11C.

1051 **Clip 6** Juvenile pike. Dye takes two routes through nasal chamber. Superior view of nasal
1052 region. Roll $+45^\circ$; camera positions a and Y. Clip rotated 180° . Compare with Fig. A.8C,
1053 Appendix A.5.

1054 **Clip 7** Adult pike. Dye takes two routes through nasal chamber. Lateral aspect. Roll 0° ; camera
1055 position a. Compare with Fig. 11D.

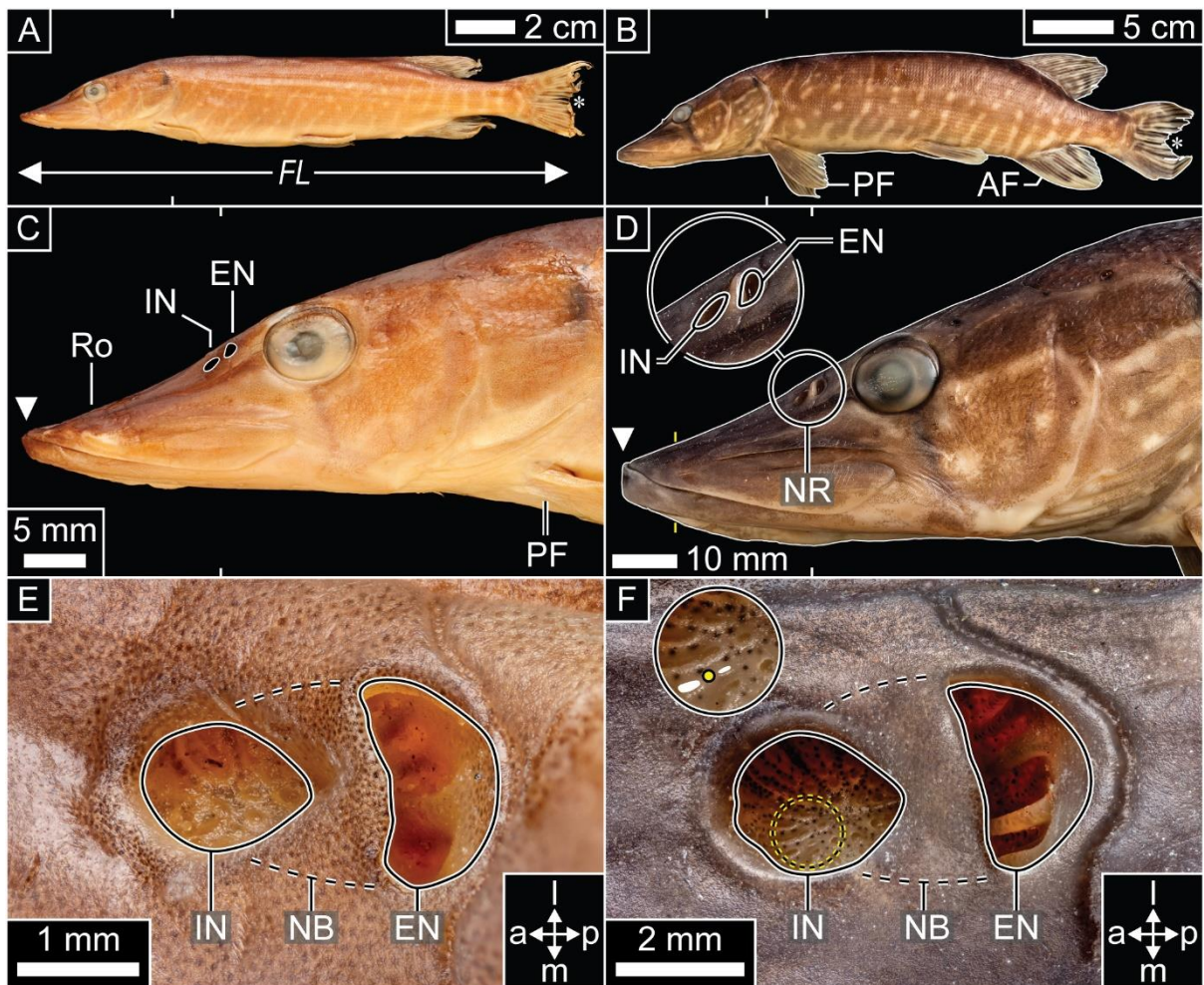
1056 **Clip 8** Juvenile pike. Vortex in incurrent nostril. Superior view of nasal region. Roll $+45^\circ$;
1057 camera positions a and Y. Clip rotated 180° . Compare with Fig. A.8D, Appendix A.5.

1058 **Clip 9** Adult pike. Vortex in incurrent nostril. Superior view of nasal region. Roll $+45^\circ$; camera
1059 position a. Clip rotated 180° . Compare with Fig. 11E.

1060 **Clip 10** Adult pike. Probable passage of dye through posterior sensory channels. Superior view
1061 of *left* nasal region. Roll $+150^\circ$; camera position a. Compare with Fig. 11F.

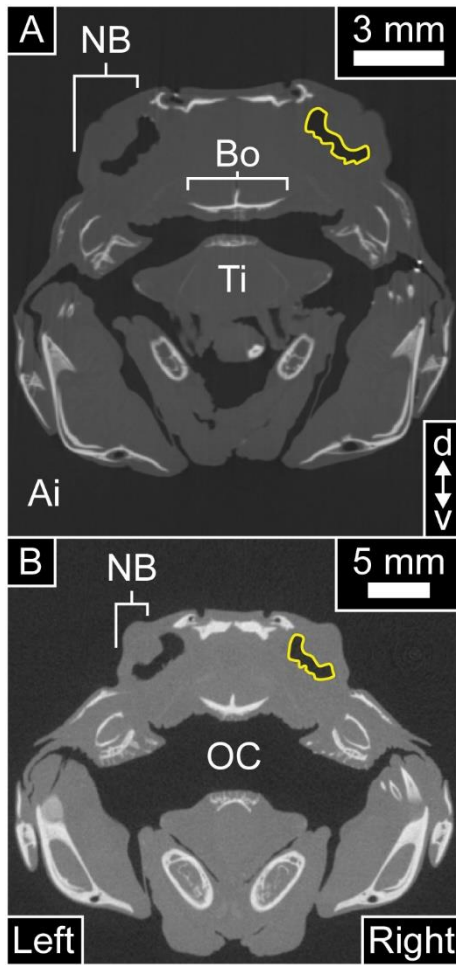
1062 **Clip 11** Adult pike. Passage of dye over nasal bridge. Lateroventral aspect. Roll -60° ; camera
1063 position a. Compare with Fig. 11G.

1064 **Clip 12** Juvenile pike. Passage of dye over excurrent nostril. Lateral aspect. Roll 0° ; camera
1065 position a. Compare with Fig. 11H.



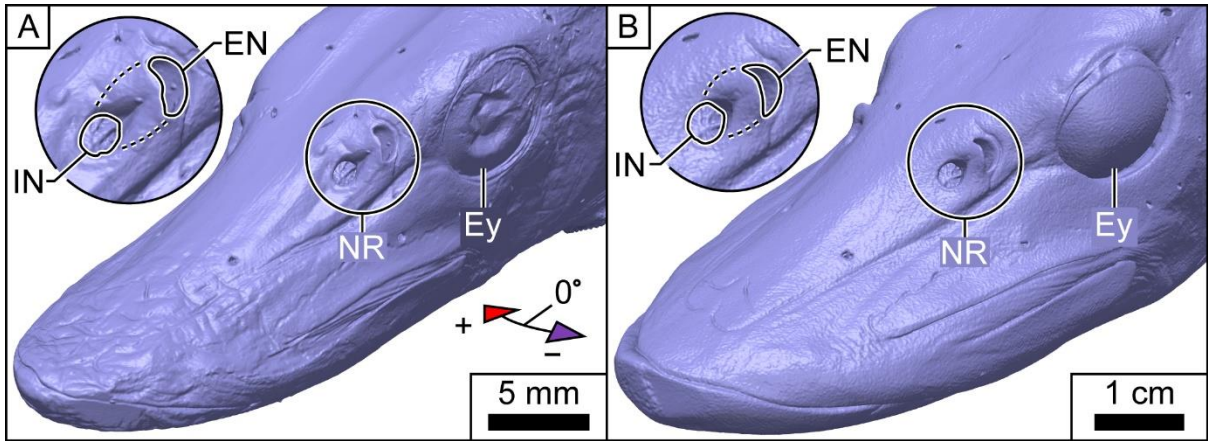
1066
 1067
 1068
 1069

Fig. 1 The two pike (*Esox lucius*) specimens used to generate the fluid dynamics models.



1070
1071
1072
1073

Fig. 2 TIFF images from micro-CT scans of (A) juvenile and (B) adult pike.



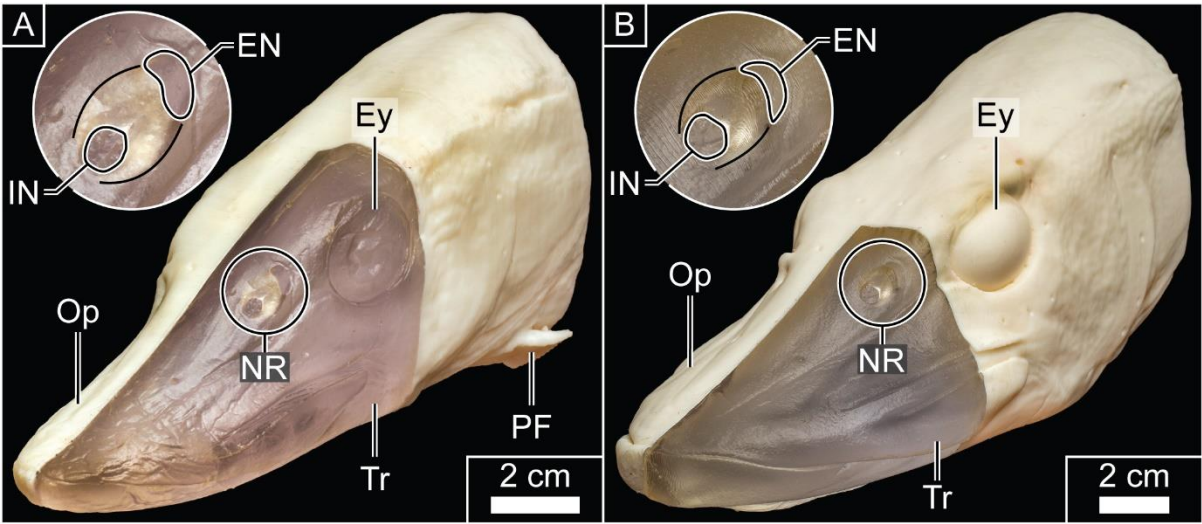
1074

1075

1076

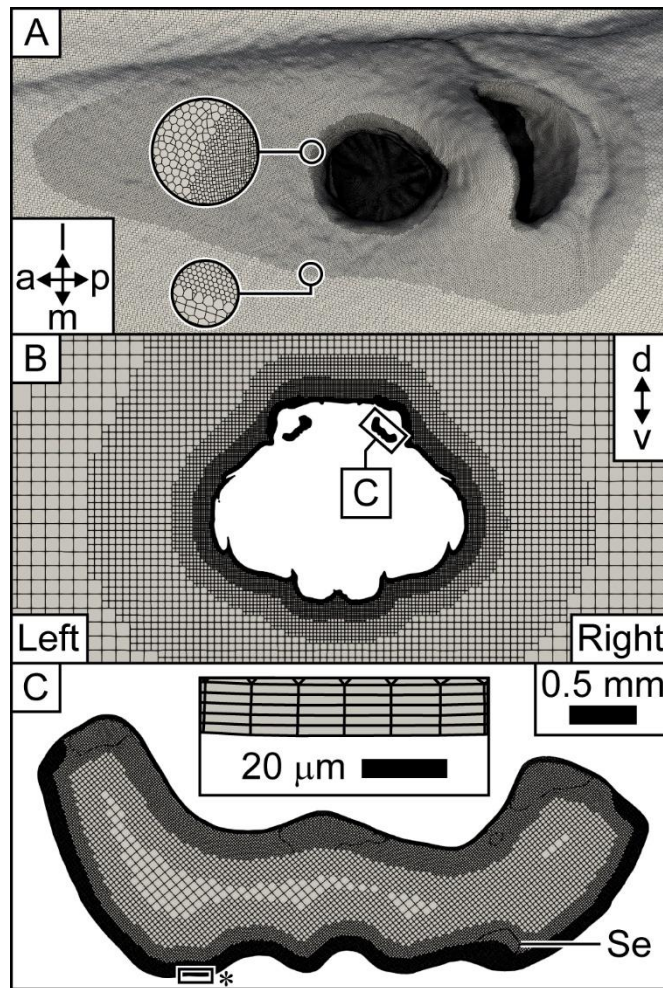
1077

Fig. 3 Surface models of heads of (A) juvenile and (B) adult pike.



1078
1079
1080
1081

Fig. 4 Plastic models of heads of (A) juvenile and (B) adult pike.



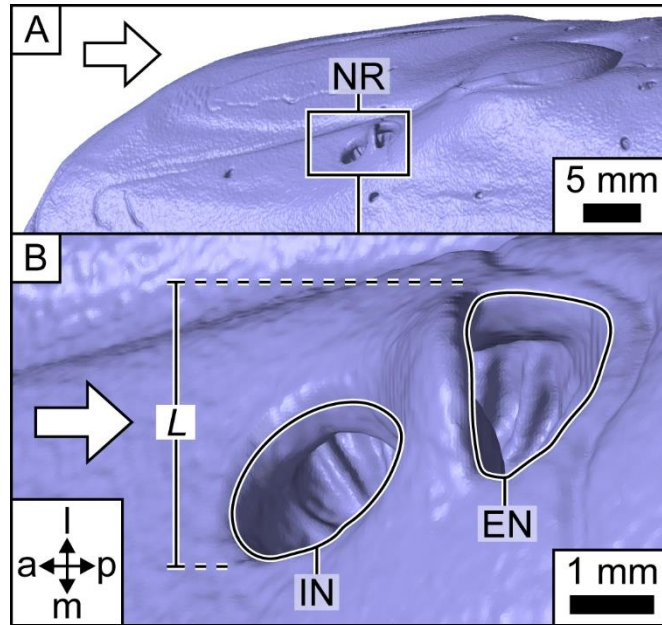
1082

1083

1084

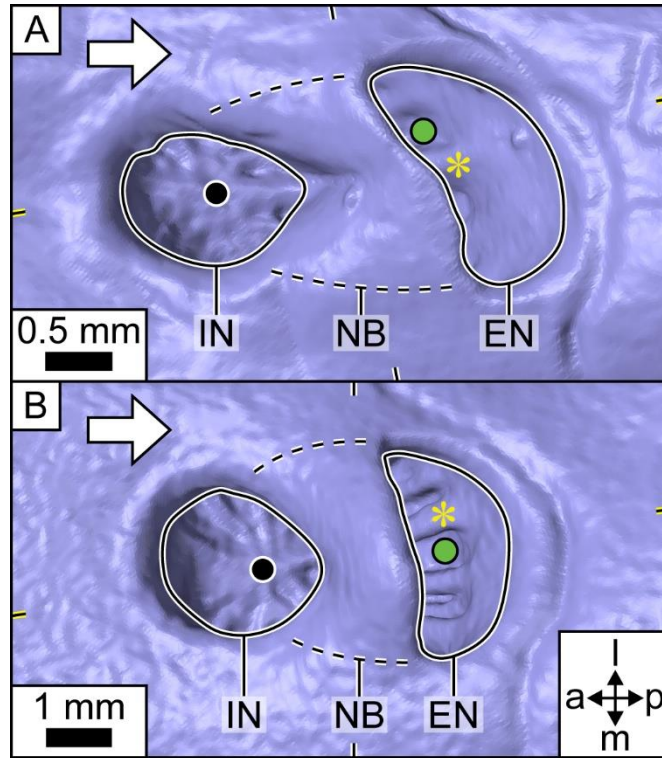
1085

Fig. 5 CFD mesh of adult pike.



1086
1087
1088
1089

Fig. 6 Characteristic dimension of adult pike's nasal region.



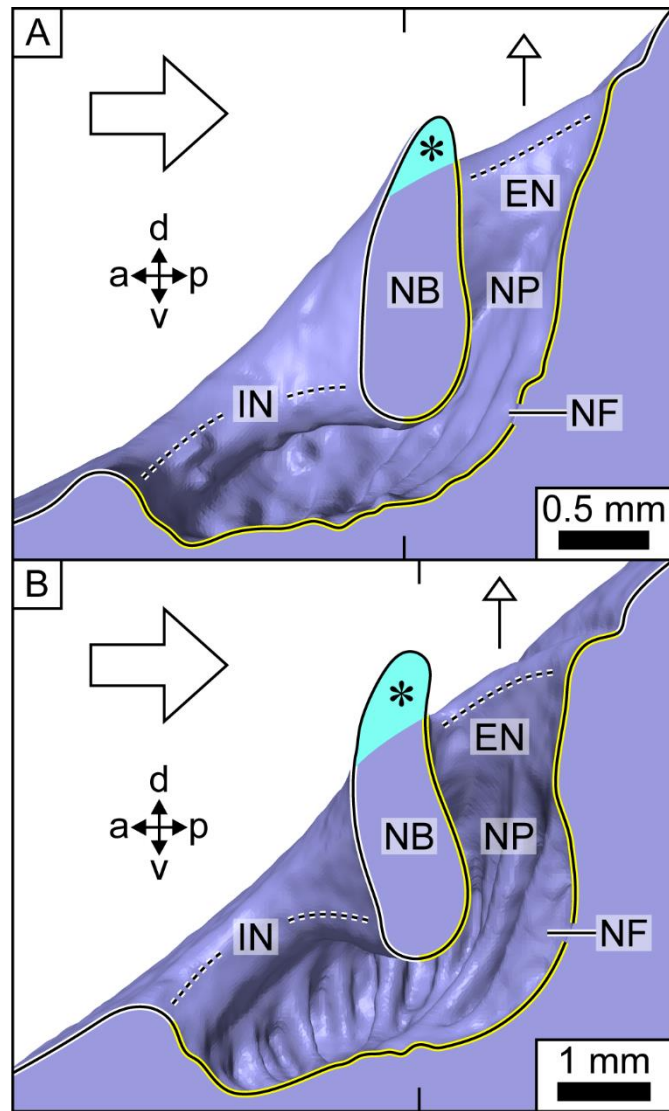
1090

1091

1092

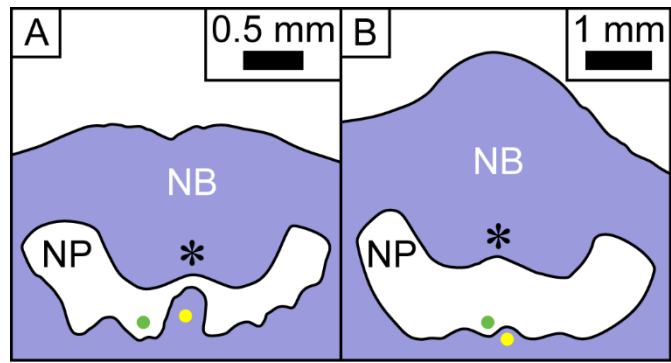
1093

Fig. 7 Detail of surface models of (A) juvenile and (B) adult pike.



1094
 1095
 1096
 1097

Fig. 8 Detail of surface models of (A) juvenile and (B) adult pike.



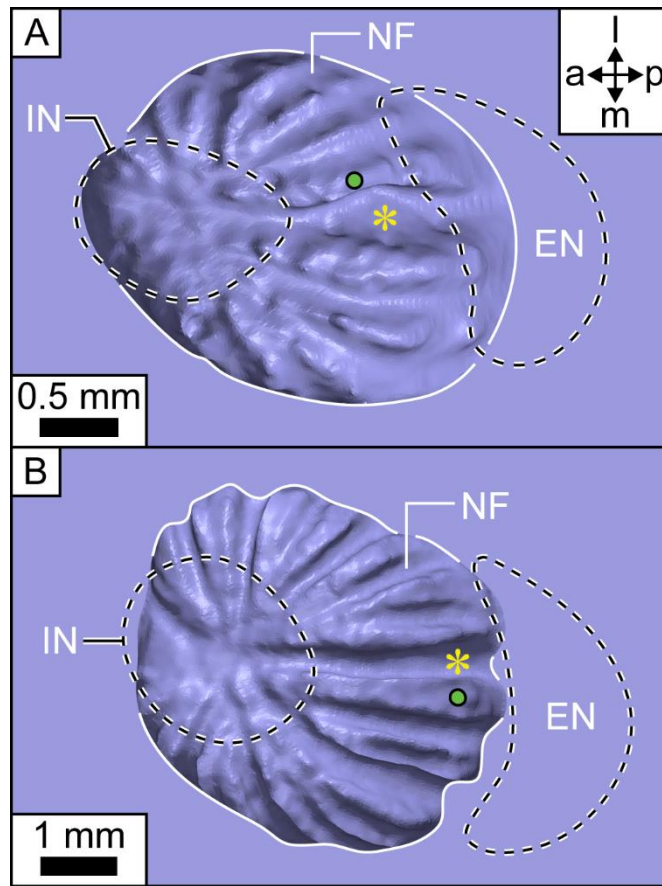
1098

1099

1100

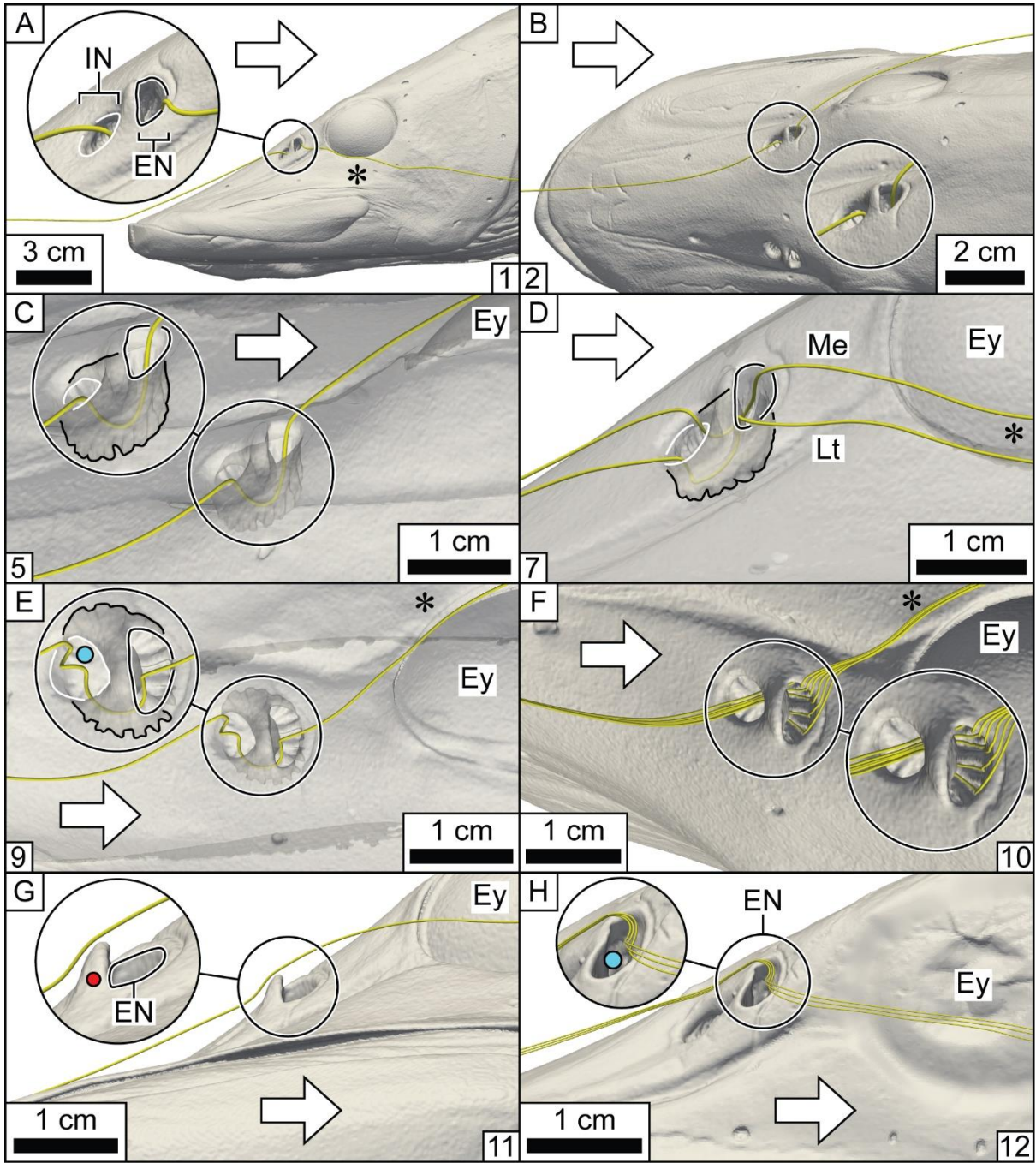
1101

Fig. 9 Detail of surface models of (A) juvenile and (B) adult pike.



1102
1103
1104
1105

Fig. 10 Detail of surface models of (A) juvenile and (B) adult pike.

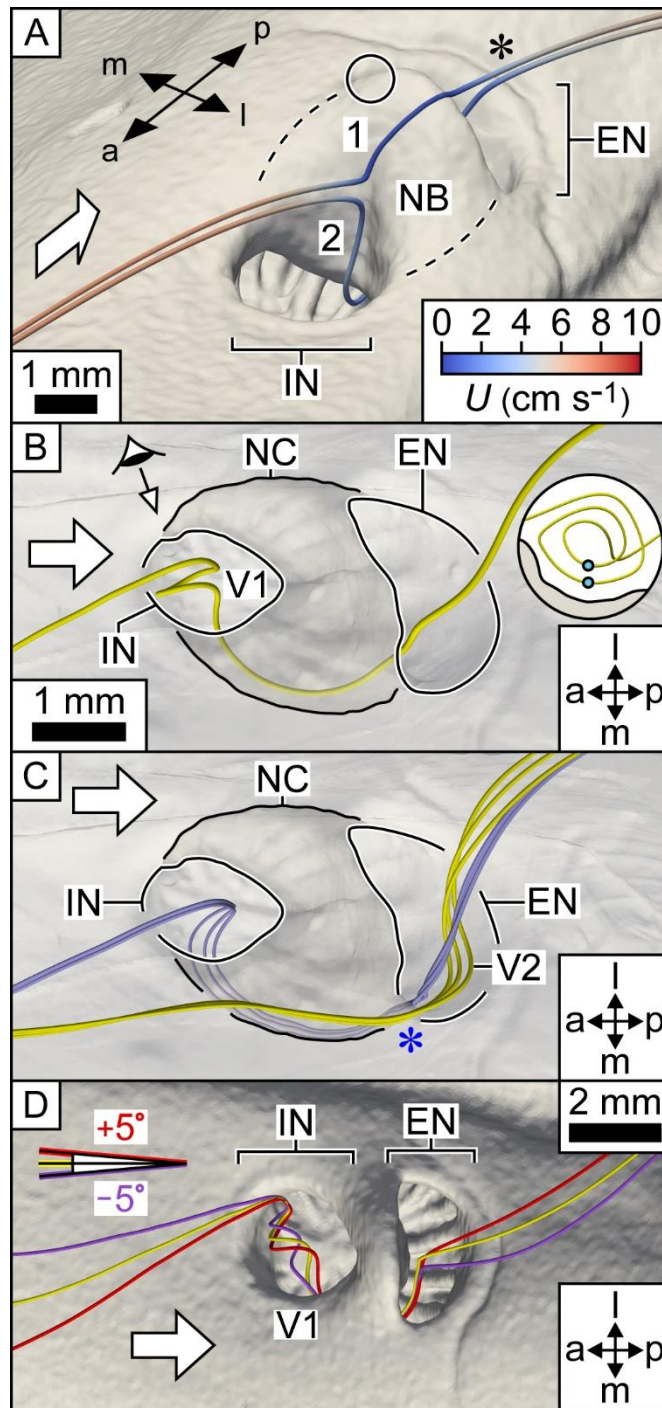


1106

1107

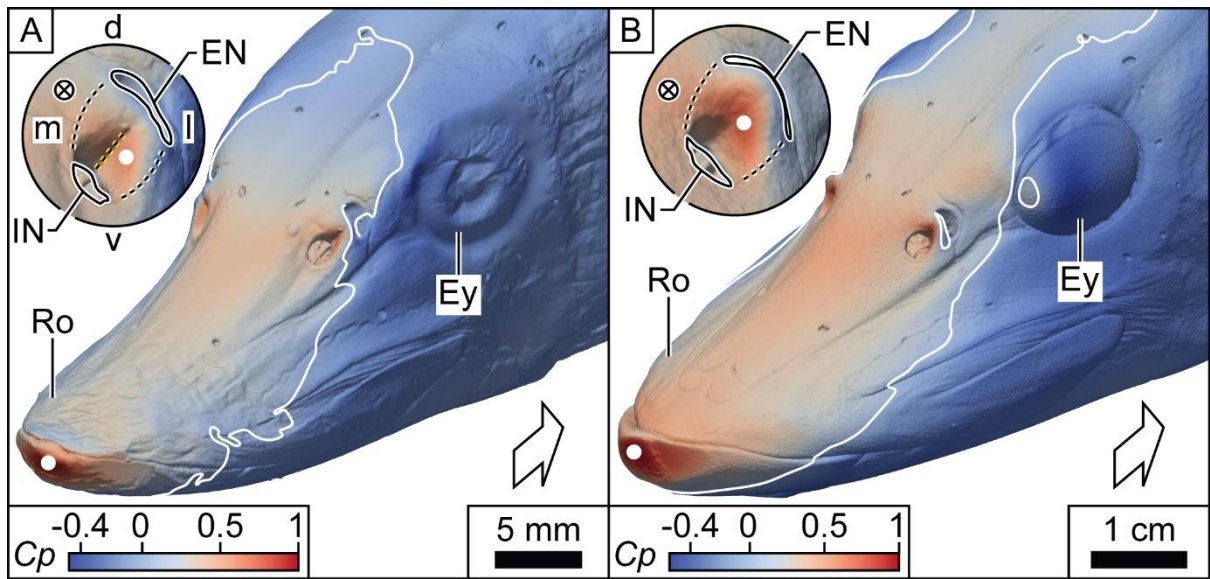
1108 **Fig. 11** Correspondence of CFD-generated streamlines to dye behaviour in the plastic models

1109 of the pike.



1110
 1111
 1112
 1113

Fig. 12 CFD-generated streamlines (tubes) in the nasal region of the pike CFD models.



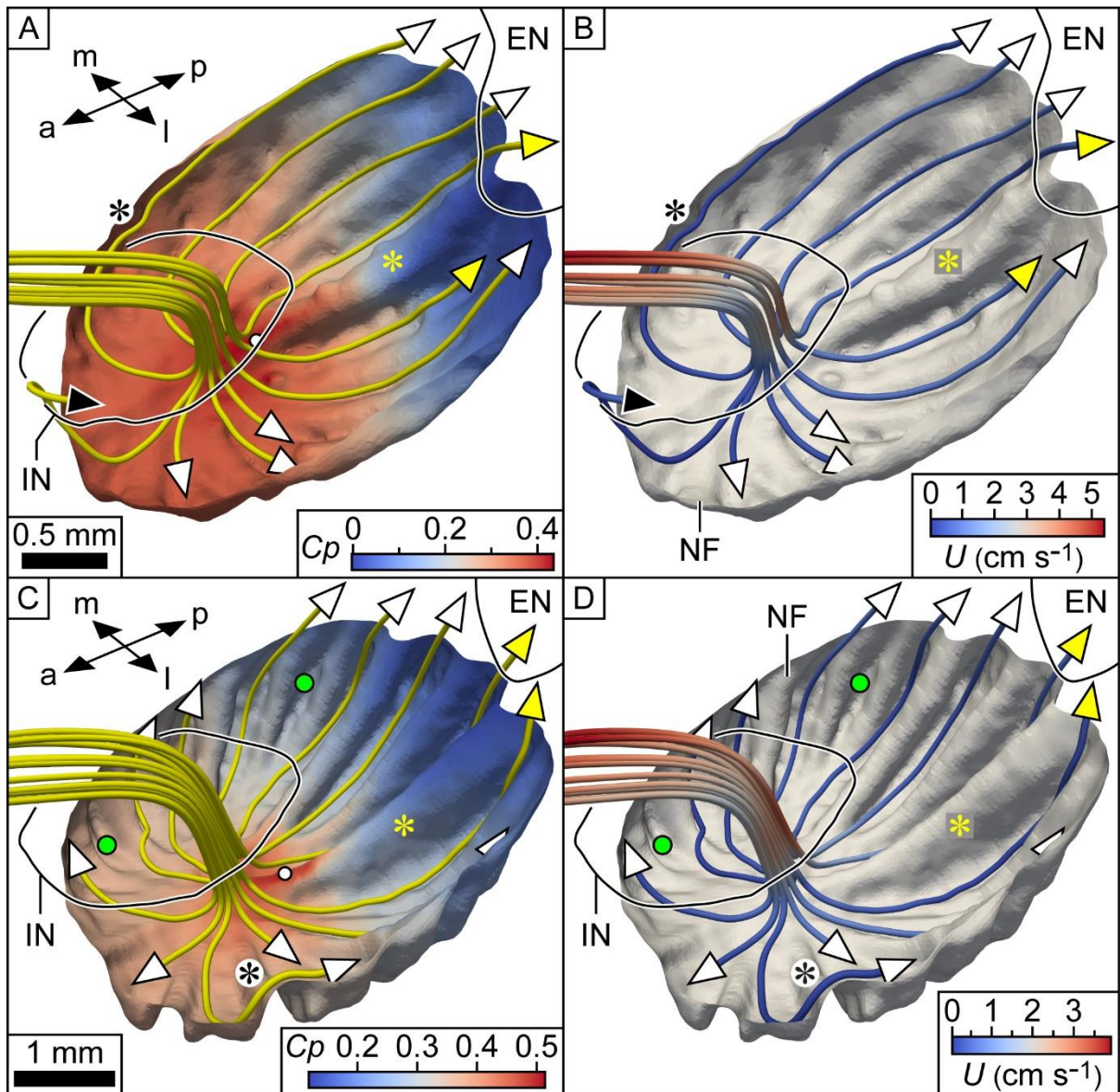
1114

1115

1116

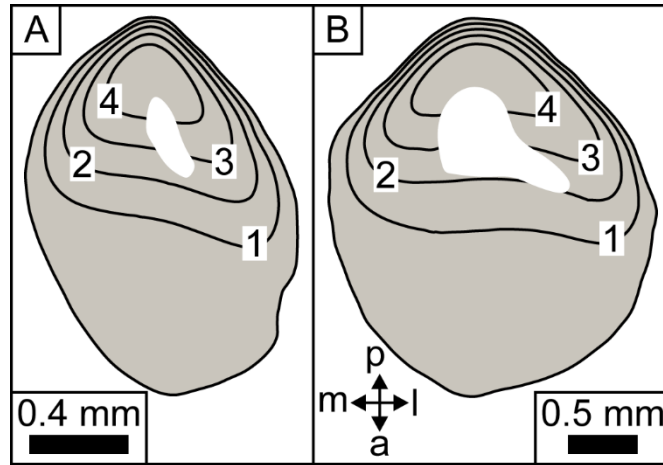
Fig. 13 Static pressure on the surface of (A) juvenile and (B) adult pike CFD models.

1117



1118
 1119
 1120
 1121
 1122

Fig. 14 CFD-generated streamlines passing through olfactory sensory channels of juvenile (A and B) and adult (C and D) pike CFD models.



1123

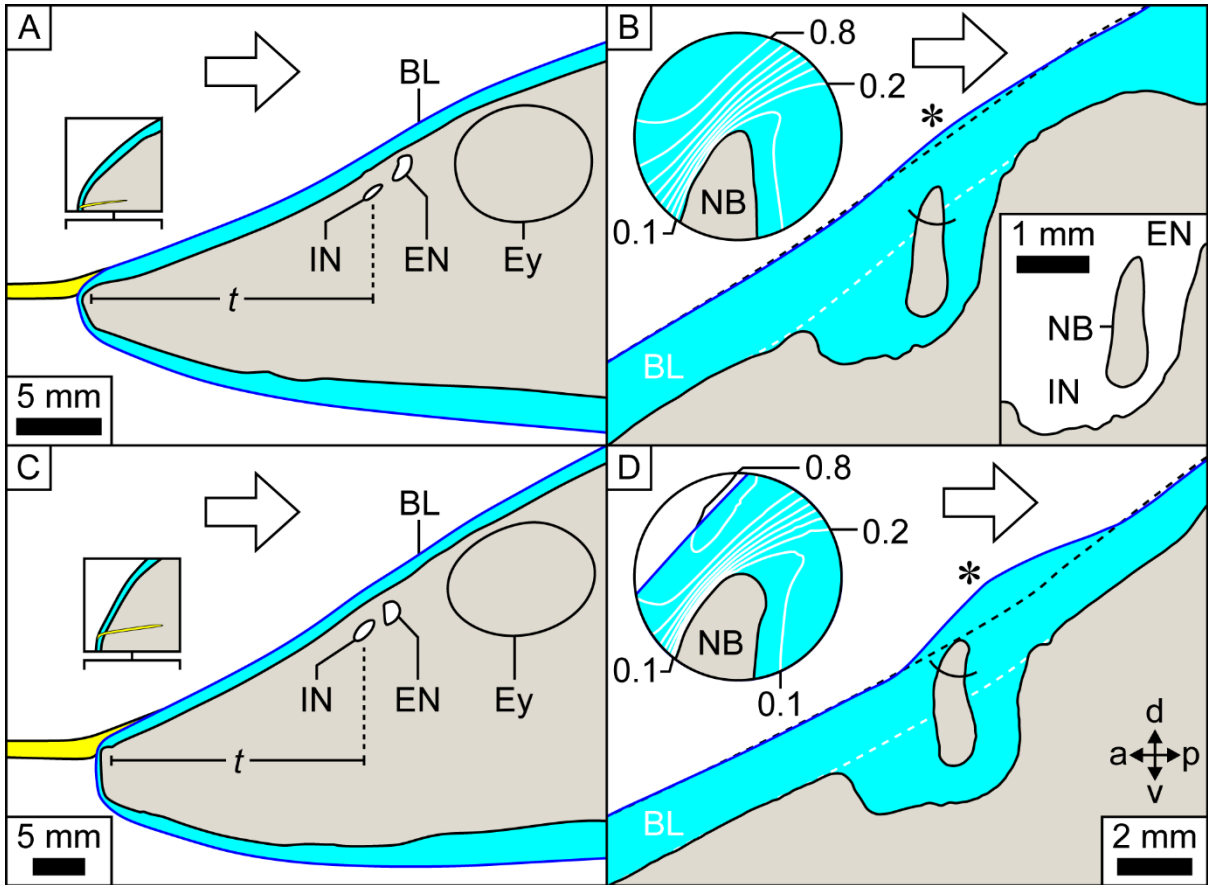
1124

1125 **Fig. 15** Incurrent nostril entry points for CFD-generated streamlines passing through the

1126 olfactory sensory channels in the nasal chamber of (A) juvenile and (B) adult pike CFD

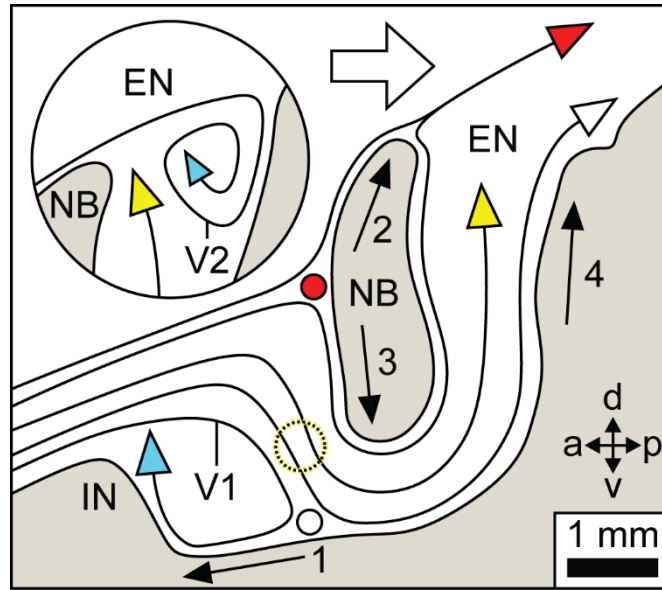
1127 models.

1128



1129
 1130
 1131
 1132

Fig. 16 Boundary layers (blue) in the pike CFD models.



1133
 1134
 1135
 1136

Fig. 17 Schematic of flow in the nasal region of the pike.

Specimen	Free-stream speed (cm s ⁻¹)	Model	Total drag of model (mN)	Percentage contribution of nasal region to total drag ^c	Percentage contributions of pressure drag (P) and viscous drag (τ) to entire model or nasal region			
					Entire model		Nasal region ^c	
					P	τ	P	τ
Juvenile	15	Wild type ^a	1.32	5.4	14	86	77	23
		Mutant ^b	1.32	5.3	14	86	77	23
Adult	10	Wild type	2.88	4.0	24	76	86	14
		Mutant	2.87	3.6	23	77	88	12

1137

1138 **Table 1** Drag forces and contributions to drag in the CFD models of juvenile and adult pike. a) Wild type: model with unaltered nasal region. b)
1139 Mutant: model in which the nostrils and nasal chamber of each nasal region have been replaced by a continuous surface that blends smoothly
1140 with the rest of the head. c) Values given are for the two *combined* nasal regions. Highlighted entries are referred to specifically in the main text.

1141

Appendix A

1142

1143

1144 *A.1. Additional methodology*

1145

1146 *A.1.1. X-ray micro-computed tomography*

1147 For the X-ray micro-computed tomography (micro-CT) scan of the juvenile pike, the
1148 specimen was held in a truncated 500 cm³ plastic measuring cylinder (height 14 cm; inner
1149 diameter 4.8 cm), with the body axis vertical and the head uppermost. To prevent the
1150 specimen undergoing unwanted movements during the scan, it was wrapped in plastic film,
1151 covering the body (but not the head) to the base of the pectoral fins, and then packed tightly
1152 against the side of the cylinder with bubble-wrap, leaving the head protruding from the top of
1153 the cylinder. Subsequently, to prevent the specimen drying out during the scan, several drops
1154 of preservative fluid (70 % industrial methylated spirits, 30 % distilled water) were put on the
1155 head and a plastic sleeve was placed over the entire arrangement. The X-ray beam was
1156 generated from a rotating tungsten reflection target. Exposure time (single image),
1157 accelerating voltage, and current were 708 ms, 90 kV, and 332 μ A, respectively. A total of
1158 2799 projections were collected in a single 360° rotation at 0.128617° intervals. The scan of
1159 the juvenile pike was also used to generate the nasal region and nasal volume models
1160 (Appendix A.2).

1161

1162 For the micro-CT scan of the adult pike, the specimen was held in a 1000 cm³ plastic
1163 measuring cylinder (height 26.5 cm; inner diameter 7.7 cm), with the body axis vertical and
1164 the head uppermost. To prevent the specimen undergoing unwanted movements during the
1165 scan, it was placed in a plastic sleeve and a strip of muslin wrapped around the *outside* of the
1166 sleeve, in the pectoral fin region (Fig. 1, PF), lodging the specimen firmly in place. (Placing
1167 the muslin inside the sleeve would have resulted in it absorbing preservative fluid from the
1168 specimen, causing the latter to shrink and therefore move during the scan.) To prevent the
1169 specimen drying out during the scan, 100 cm³ of preservative fluid was added to the plastic
1170 sleeve, such that the level of fluid was just below the posterior edge of the anal fins (Fig. 1B,
1171 AF). A plastic sleeve was placed over the head (without touching it) for the same purpose.
1172 We left the specimen in this arrangement for 4 hours before performing the scan, to allow
1173 excess preservative fluid to drain from the nasal chamber. (Excess preservative fluid,
1174 particularly between the nasal folds [e.g. Fig. 14D], would have blurred the surface of the

1175 specimen in the resultant scan, because pixels corresponding to preservative fluid have
1176 similar intensities to pixels corresponding to tissue stored in preservative fluid.) The X-ray
1177 beam was generated from a static tungsten reflection target and passed through a 0.5 mm
1178 copper filter. Exposure time (single image), accelerating voltage, and current were 708 ms,
1179 170 kV, and 70 μ A, respectively. A total of 3142 projections were collected in a single 360°
1180 rotation at 0.114577° intervals.

1181

1182 A second, higher resolution, micro-CT scan of the adult pike was used to generate the (right)
1183 nasal region and nasal volume models (Appendix A.2). The mounting conditions and X-ray
1184 parameters for the second scan were the same as the first. The second scan comprised 1747
1185 TIFF images and had a voxel size of 32.5 μ m x 32.5 μ m x 32.5 μ m ([dataset] Garwood et al.,
1186 2020b).

1187

1188 Projections from the three scans were transformed into a three-dimensional matrix using CT-
1189 Pro (Nikon Metrology, Tring, UK). The scans were converted into 8-bit TIFF images using
1190 VGStudio MAX (Version 2.2, Volume Graphics GmbH, Heidelberg, Germany) for the
1191 juvenile pike and Drishti (Version 2.6.3; Limaye, 2012) for the adult pike.

1192

1193 *A.1.2. Surface models*

1194 Surface models of the heads of the pike specimens were created as follows. TIFF images
1195 from each micro-CT scan were imported into ScanIP and segmented with the Threshold tool,
1196 creating a ‘mask’ of the complete head (‘head’ mask). For thresholding, we chose a lower
1197 value of either 53 (juvenile pike) or 55 (adult pike) and an upper value of 255. These values
1198 were chosen because they gave masks with smooth surfaces whilst preserving the anatomical
1199 detail of the nasal regions. Internal cavities (e.g. the oral cavity [Fig. 2B, OC] and the lateral
1200 line canals [Fig. A.1A, filled yellow regions; Fig. 6.2A of Helfman et al., 2009]) were filled
1201 using the Floodfill and Paint tools. (The internal cavities were filled to reduce the size of the
1202 stereolithography [STL] file prior to 3D printing/conversion to the computational fluid
1203 dynamics mesh.) The head mask was adjusted to either a) life size, b) 3x life size (juvenile
1204 pike), or c) 2x (adult pike) life size with the Rescale tool.

1205

1206 We performed additional image processing on the head mask of the adult pike. First, the head
1207 mask was smoothed with a Recursive Gaussian filter (sigma x, y and z values: one pixel, for

1208 the same reason that we chose the thresholding values). Next, a relatively small protrusion on
1209 the dorsal surface of the head mask was removed using the Paint tool . Based on a region of
1210 intense pixels at this point in the micro-CT scan (Fig. A.1C, circle), together with a visual
1211 inspection of the specimen, we surmise that the protrusion was caused by a fragment of metal
1212 or glass. The amended surface, together with a micro-CT artifact on the rostral tip, was then
1213 smoothed using the 3D editing tool (Cylinder for amended surface, Cuboid for rostral tip)
1214 (Fig. A.1D, circle, and Fig. A.2). The artifact on the rostral tip probably arose from at that
1215 point a combination of noise and poor contrast between the air and the specimen.

1216

1217 Two new masks were created from the larger-than-life head masks of the juvenile and adult
1218 pike: an ‘opaque’ mask corresponding to each plastic model’s opaque part (Fig. 4, Op); and a
1219 ‘translucent’ mask corresponding to the translucent part (Fig. 4, Tr). The translucent mask
1220 was isolated from the head mask with the Floodfill tool. The opaque mask was generated
1221 with the Boolean operations tool by subtracting the translucent mask from the head mask.
1222 The Paint tool was used to put a hole in the back of the opaque mask (for the plastic model’s
1223 aluminium peg, Fig. A.3A, Pe). To generate an STL model of manageable size for 3D
1224 printing, the pixel spacing of the opaque mask of the juvenile pike was adjusted to 59 μm
1225 with the Resample tool. The opaque mask of the adult pike was not, however, resampled. A
1226 surface model was created from each of the three types of mask (head, opaque, translucent)
1227 with the following features (de)selected in ScanIP’s ‘Model configuration’ dialogue box: a)
1228 ‘General’ tab \rightarrow Smart mask smoothing (pre-processing) \rightarrow Use greyscale values; b)
1229 ‘Surface settings’ tab \rightarrow Triangle smoothing \rightarrow Use triangle smoothing for masks (10
1230 iterations); and c) ‘Surface settings’ tab \rightarrow Decimation \rightarrow Decimate box: 10 % for opaque
1231 and translucent masks of juvenile pike, unticked for all other masks. The surface models were
1232 then each exported in binary format as STL files.

1233

1234 STL files of the nasal regions and nasal volumes (a nasal volume being the space occupied by
1235 water in the nasal chamber) were created using the same methodology as above (see also
1236 Appendix A.1.5 of Garwood et al., 2019).

1237

1238 *A.1.3. Plastic models*

1239 The two parts of each plastic model of the pike’s head were 3D printed from the
1240 corresponding STL files according to the methodology of Abel et al. (2010). The opaque part

1241 (Fig. 4, Op) of each model was made in off-white plastic (ABS for the juvenile pike, ASA for
1242 the adult pike; both Stratasys, Eden Prairie, USA), to give good contrast with the red dye
1243 used to visualise flow. The translucent part of each model, which included the right nasal
1244 region (Fig. 4, Tr), was made in VisiJet SL Clear plastic (3D Systems, Rock Hill, South
1245 Carolina, USA), to facilitate dye visualisation within the nasal chamber. For both models we
1246 chose the right nasal region for the translucent part, either because its excurrent nostril was
1247 better defined than that of the left nasal region (juvenile pike) or because its nasal folds were
1248 more pronounced than those in the left nasal region (adult pike). The thickness of the layers
1249 arising from the 3D printing process was either 178 μm (opaque part) or 50 μm (translucent
1250 part). The appropriate opaque part and translucent part were glued together to give a
1251 complete model (Fig. 4). An aluminium peg (Fig. A.3A, Pe; see also Fig. 4 of Garwood et al.,
1252 2019) was inserted into the back of each model, allowing the model to be fixed to the rig used
1253 to suspend it in the flume.

1254

1255 Plastic models of the nasal regions and nasal volumes were 3D printed using the above
1256 methodology. Each plastic model of a nasal region comprised two parts: the nasal region
1257 minus the nasal bridge, and the nasal bridge. The plastic model of the nasal bridge fitted into
1258 the plastic model of the nasal region to give a model of the complete nasal region. The ability
1259 to remove the nasal bridge from the complete model helped determine the detailed
1260 arrangement of nasal folds (Appendix A.2). The plastic models of the nasal regions/volumes
1261 were 12.5x (juvenile pike) and 5x (adult pike) life size, and were made in off-white plastic
1262 (ASA).

1263

1264 *A.1.4. Environmental currents likely to be encountered by a stationary pike*

1265 The current in either a lake, or a slow-flowing stream, or a river, all typical freshwater
1266 habitats of a pike (Chapman and Mackay, 1984; Masters et al., 2002), is $\leq 30 \text{ cm s}^{-1}$ (Horne
1267 and Goldman, 1994, p. 72; James et al., 2005, p. 108; Macan, 1974, p. 32).

1268

1269 *A.1.5. Cruising speed of a pike*

1270 The pike that we observed at the Aquarium of the Lakes cruised (Webb, 1984) at speeds in
1271 the range 8 – 24 cm s^{-1} (average = 15 cm s^{-1} , $n = 11$), corresponding to 0.08 – 0.3 $FL \text{ s}^{-1}$ ($FL =$
1272 75 – 100 cm; Section 2.2). Webb (1984) gives a range of cruising speeds for the pike of 1 – 4
1273 body lengths s^{-1} . Assuming body length is total length (Fig. 2.2 of Helfman et al., 2009), and

1274 given that in the pike total length is essentially fork length (Fig. 1A), these data give a range
1275 of cruising speeds of $0.08 - 4 FL s^{-1}$.

1276

1277 *A.1.6. Dye visualisation*

1278 The working section (L x W x H) of the Eidetics Model 1520 flume was 152 cm x 38 cm x
1279 51 cm. Each model was suspended in the flume via its aluminium peg using the rig described
1280 in Abel et al. (2010). The rig/peg arrangement also allowed the roll (Fig. 10.1 of Barnard and
1281 Philpott, 2004) of the model to be varied (Fig. A.3A, R1). The model was positioned such that
1282 it was central (± 2 cm) width-wise to the working section of the flume. The maximum
1283 transverse cross-sectional area of each model was 36 cm^2 (juvenile pike) and 64 cm^2 (adult
1284 pike), both less than 5 % of the working cross-sectional area of the flume. The effect from the
1285 walls of the flume on flow in the vicinity of the model should therefore have been negligible,
1286 based on standard corrections (Barlow et al., 1999, p. 361). The model of the juvenile pike
1287 was illuminated with a quartz lamp fitted with a white screen to diffuse light; that of the adult
1288 pike was illuminated with a halogen lamp. White card was placed behind each model to help
1289 visualise dye. The dye solution was introduced from a pressurised reservoir using stainless
1290 steel tubing (internal diameter 1.3 mm; external diameter 2 mm). The horizontal section of
1291 this tubing, from which dye was released, was 27 cm (juvenile pike) or 25 cm (adult pike)
1292 from the flume's floor. At a free-stream speed of 5 cm s^{-1} , dye emerged from the tubing as a
1293 well-defined filament, indicating that the exit velocity of the dye was equal to the local flow
1294 velocity (Fig. 3.1 of Lim, 2000). To minimise the effect of the tubing on flow over the
1295 models (Lim, 2000), the aperture of the tubing was located some distance (juvenile pike: 5
1296 cm; adult pike: 12 – 16 cm) upstream from the point of impingement on the model. The dye,
1297 as a filament, was directed at the anterior rostral edge of each model (Video clip 1).

1298

1299 *A.1.7. Computational fluid dynamics*

1300

1301 *A.1.7.1. Simulations*

1302 Each mesh for a computational fluid dynamics (CFD) simulation was derived from the STL
1303 model of the respective head (Appendix A.1.2). Before converting the STL models to CFD
1304 meshes, we modified them in several ways. First, we added a tapered extension ('tail') to the
1305 back of each STL model (Fig. A.4, Ta). The tails were approximately 4x (juvenile pike) or 5x
1306 (adult pike) the length of the head; each had a 7° taper (Fig. A.4). We added each tail to

1307 prevent flow separating from the back of the head, and to reduce therefore any modification
1308 to upstream flow due to the lack of a body (Garwood et al., 2019). Second, we smoothed the
1309 rim of each eye, in order to avoid the formation of small pockets within the subsequent mesh.
1310 Such pockets may have caused the simulations to stop prematurely. Finally, in the model of
1311 the juvenile pike, we removed the base of each pectoral fin (Appendix A.3). We made the
1312 modifications using GeoMagic Wrap (3D Systems; Appendix A.1.4.2 of Garwood et al.
1313 2019). Each STL model was converted to a CFD mesh with the snappyHexMesh utility of the
1314 software OpenFOAM (Weller et al., 1998). The computational domains for the simulations
1315 had a velocity inlet and a pressure outlet. The dimensions (L x W x H) of the computational
1316 domains were 10.9 m x 2.1 m x 2.1 m (juvenile pike), and 30.0 m x 5.6 m x 5.6 m (adult
1317 pike). Each model lay at the centre of the domain in the transverse plane. The rostral tips
1318 were positioned 4.3 m (juvenile pike) or 11.9 m (adult pike) from the velocity inlet. The size
1319 of the computational domain, together with the position of the model within it, were chosen
1320 to minimise flow artifacts from the walls of the domain. The no-slip condition was set for all
1321 solid surfaces, together with a symmetry plane (with a zero gradient of velocity and pressure
1322 across the plane) at the dorsal, ventral, and lateral surfaces of the domain. The Navier-Stokes
1323 equations governing transient laminar flow were solved with the OpenFOAM algorithm
1324 PIMPLE. The Navier-Stokes equations governing steady laminar flow were solved with the
1325 OpenFOAM algorithms SIMPLE (juvenile pike) and SIMPLEC (adult pike), respectively.
1326 Solutions to the Navier-Stokes equations gave a field of velocity vectors.

1327

1328 The terms UMean, pMean, and tauMean in Appendices A.1.7.3, A.1.7.5 and A.1.7.6 are the
1329 average velocities, static pressure, and shear stress over the last 500 iterations of the
1330 converged, time-averaged solution to the Navier-Stokes equations for a given simulation. The
1331 units of pMean and tauMean when generated by the simulation are energy per unit mass.
1332 Therefore, to convert pMean and tauMean to the units of pressure (pascals), both must be
1333 multiplied by the density of water.

1334

1335 *A.1.7.2. Pressure*

1336 Points of relatively high static pressure on the surface of a CFD model were located using
1337 ParaView's Find Data tool.

1338

1339 The average static pressure in each nostril ($P - P_0$ in Equation 1 of the main text) was
1340 calculated in ParaView by using the Slice filter to put through the mesh a plane that passed

1341 through the nostril, and then applying to that plane the following succession of filters:
1342 Connectivity → Threshold (to isolate the segment of the plane in the nostril) → Calculator
1343 (to calculate the static pressures at all points within this segment) → Integrate Variables. The
1344 average static pressure in the segment was then found by dividing the ‘pressure’ entry
1345 (Attribute: Point Data) in the Spreadsheet view by the Area entry (Attribute: Cell Data).

1346

1347 Note that Equation 2 (main text) is a more rigorous way of expressing the pressure difference
1348 across the nostrils than the one we used in our work on the sturgeon, *Huso dauricus*
1349 (Garwood et al., 2019). In the latter, for C_p (Incurrent nostril) we used the maximum static
1350 pressure in the nasal region (located on the lateral wall of the incurrent nostril of *H. dauricus*;
1351 Fig. 11B of Garwood et al., 2019). Ideally, the pressure difference across the nostrils should
1352 be calculated using the incurrent and excurrent faces of a control volume (Massey, 1989, p.
1353 115), here the incurrent and excurrent faces of the nasal volume. Using Equation 2, we
1354 recalculated ΔC_p for *H. dauricus*, in order to compare it with ΔC_p for the juvenile and adult
1355 pike.

1356

1357 *A.1.7.3. Streamlines*

1358 Streamlines were generated in ParaView by first applying the Stream Tracer With Custom
1359 Source filter to a point, with the following menu selections (selections in brackets): Vectors
1360 (UMean); Interpolator Type (Interpolator with Point Locator); Integration Direction (Both);
1361 Integrator Type (Runge-Kutta 4.5); Integration Step Unit (Cell Length); Initial Step Length
1362 (0.2 m); Minimum Step Length (0.01 m); Maximum Step Length (0.5 m); Maximum Steps
1363 (2000); Maximum Streamline Length (0.2 m); Terminal Speed (10^{-12} m s⁻¹); Maximum Error
1364 (10^{-6}). The Tube filter was then applied to the Stream Tracer With Custom Source filter, with
1365 the following menu selections (selections in brackets): Scalars (Angular Velocity); Vectors
1366 (Normals); Number of Sides (6); Radius (juvenile pike: typically 2×10^{-5} m; adult pike:
1367 typically 3.5×10^{-5} m). Points were created from the Sources menu (Point Source).

1368

1369 *A.1.7.4. ‘Mutant’ models*

1370 Mutant models (Fig. A.7B and D; Section 2.4) were generated with GeoMagic Wrap (3D
1371 Systems), as follows. First, the polygons bounding each nasal region were selected with the
1372 Paint Brush Selection tool (Select Visible button active) and then removed (Polygons →
1373 Delete command). Next, the isolated nasal region was deleted (Paint Brush Selection tool →

1374 select a group of polygons within the isolated nasal region → Bounded Components →
1375 Delete). Finally, the nasal region was replaced with a continuous surface (Polygons → Fill
1376 Holes → Fill Single → Complete → Curvature, with the nasal region boundary selected).
1377 The resultant surface mimicked the curvature of the head in the nasal region.

1378

1379 *A.1.7.5. Boundary layer*

1380 The vorticity contour used to gauge the thickness of the boundary layer on the surface of a
1381 model was generated in ParaView by applying the following succession of filters to the fluids
1382 file (selections in brackets): Compute Derivatives (Vectors: UMean; Output Vector Type:
1383 Vorticity; Output Tensor Type: Vector Gradient); Cell Data to Point Data; Calculator (Result
1384 Array Name: Vorticity; subsequent box entry: mag(Vorticity)); Slice (optional); Contour
1385 (Contour by: Vorticity; Value Range: 5 [i.e. 5 s⁻¹]).

1386

1387 The boundary layers in Fig. 16A and C were created by superimposing the head on the three-
1388 dimensional boundary layer generated by the method above. Each yellow region in Fig. 16A
1389 and C is the space occupied by 10 streamlines generated from a line of 10 regularly spaced
1390 points across (in the transverse sense) the right incurrent nostril. The radius of each
1391 streamline was 2 x 10⁻⁵ m (juvenile pike) or 5 x 10⁻⁵ m (adult pike).

1392

1393 The time taken (t , Fig. 16A and C) for a fluid particle to get from the point of entry into the
1394 boundary layer to the incurrent nostril was estimated as follows. First, from the Sources menu
1395 (Point Source), we put 10 uniformly scattered points in the mesh plane through the incurrent
1396 nostril (Appendix A.1.7.2). From each point we then created a streamline (Appendix A.1.7.3;
1397 Integration Direction: Backward). Using the Hover Points On function, we then identified the
1398 point at which the streamline entered the boundary layer, and read the integration time from
1399 the Spreadsheet view.

1400

1401 *A.1.7.6. Drag*

1402 Pressure drag and viscous drag were estimated in ParaView by applying the following series
1403 of filters to the surfaces.case file of a CFD model, or a segment of this model (isolated from
1404 the surfaces.case file with the Extract Block filter): 1) Extract Surface; 2) Generate Surface
1405 Normals; 3) Calculator (Result Array Name: Pressure; subsequent box entry:
1406 density*pMean); 4) Calculator (Result Array Name: Pressure Normals; subsequent box entry:

1407 Pressure*Normals); 5) Calculator (Result Array Name: Shear Stress; subsequent box entry:
1408 density*tauMean); 6) Surface Vectors (Select Input Vectors: Shear Stress; Constraint Mode:
1409 Parallel); 7) Integrate Variables. Pressure drag was the first entry in the row of three values
1410 under the heading ‘Pressure Normals’ in the Spreadsheet view (i.e. pressure drag in the x -
1411 direction); viscous drag was the first entry in the row of three values under the heading ‘Shear
1412 Stress’ in the Spreadsheet view (i.e. viscous drag in the x -direction).

1413

1414 *A.2. Detailed arrangement of nasal folds in the olfactory rosette*

1415 To compare the detailed arrangement of nasal folds in the right olfactory rosette of the
1416 juvenile and adult pike with the description given by Holl (1965), we used larger-than-life
1417 plastic models of both a) the nasal region and b) the nasal volume (Fig. A.10; Appendix
1418 A.1.3). We counted 12 folds in the juvenile pike (Fig. A.10A). We were unable, however, to
1419 distinguish (using Holl’s terminology) main folds from adjacent folds in the juvenile pike. In
1420 the adult pike, we counted nine main folds, and were able to identify several type II folds and
1421 one type III fold (Holl, 1965; Fig. A.10B, red disks and black disk, respectively). In both the
1422 juvenile and the adult pike we were able to identify the fold likely to have developed first in
1423 the olfactory rosette (Fig. A.10, nasal fold 1; Holl, 1965). In the main text we refer to this
1424 fold as the central posterior nasal fold.

1425

1426 *A.3. Further limitations of the models*

1427 Two further limitations of the models are:

1428

1429 1) The translucent part of the plastic model of the juvenile pike included the eye, but that of
1430 the adult pike (to make the model affordable) did not (Fig. 4).

1431

1432 2) The base of the pectoral fin was present in the plastic model of the juvenile pike (Fig. 4A,
1433 PF), but removed from the corresponding CFD model (Fig. A.4A, circle).

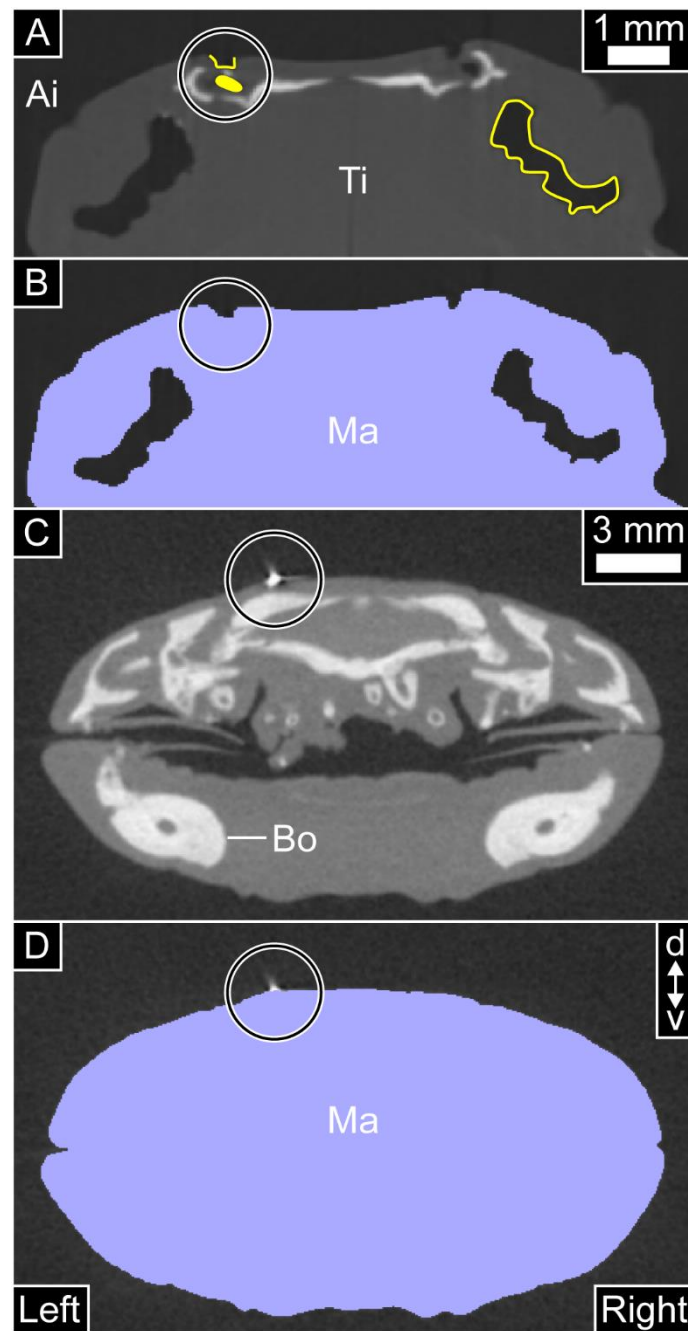
1434

1435 Given that the key elements of the pike’s olfactory flow (Section 4.3) were present in both
1436 the dye visualisation experiments and the CFD simulations, neither difference is likely to
1437 have had a significant effect on olfactory flow.

1438

1439 A.4. Additional references

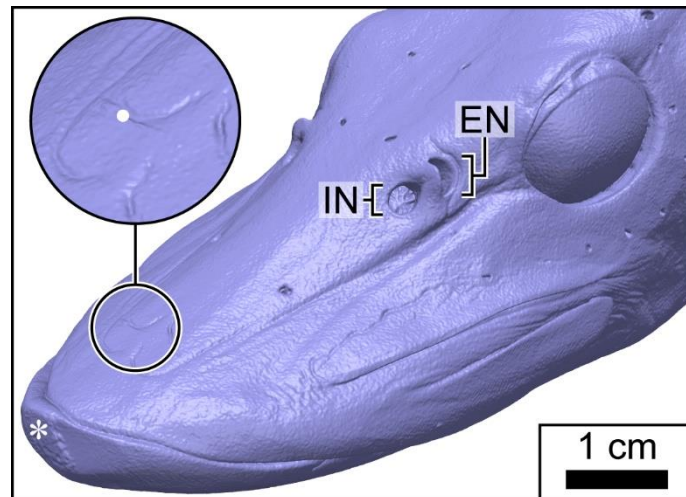
- 1440 Barlow, J.B., Rae, W.H., Pope, A., 1999. Low-Speed Wind Tunnel Testing. 3rd ed. John
1441 Wiley & Sons, New York.
- 1442 Garwood, R.J., Behnsen, J., Maclaine, J.S., Cox, J.P.L., 2020b. TIFF images from X-ray scan
1443 of nasal regions of *Esox lucius* (adult). Mendeley Data, v1.
1444 <http://dx.doi.org/10.17632/zwk97m2y66.1>.
- 1445 Horne, A.J., Goldman, C.R., 1994. Limnology. 2nd ed. McGraw-Hill, New York.
- 1446 James, R., Bennett, S., Neal, C., 2005. Water. The Open University, Milton Keynes.
- 1447 Lim, T.T., 2000. Dye and smoke visualization. In: Smits, A.J., Lim, T.T. (Eds.), Flow
1448 Visualization. Imperial College Press, London, pp. 43-72.
- 1449 Limaye, A., 2012. Drishti: a volume exploration and presentation tool. In: Stock, S.R. (Ed.),
1450 Proceedings SPIE 8506, Developments in X-ray Tomography VIII, 85060X.
- 1451 Macan, T.T., 1974. Freshwater Ecology. 2nd ed. Longman, London.
- 1452



1457 **Fig. A.1.** Image processing. (A) Dorsal part of TIFF image shown in Fig. 2A (from micro-CT
 1458 scan of juvenile pike). Circle highlights lateral line pore (broken yellow line) and lateral line
 1459 canal (filled yellow region). Continuous yellow line: perimeter of nasal chamber. (B) Same
 1460 image as (A), with mask superimposed. (C) TIFF image from micro-CT scan of adult pike
 1461 (transverse cross-section through head; location indicated by yellow marks in Fig. 1D). Circle
 1462 highlights a feature caused possibly by a fragment of metal or glass. (D) Same image as (C),

1463 with smoothed mask superimposed. Ai: Air; Bo: bone; d: dorsal; Ma: mask; Ti: tissue; v:
1464 ventral.
1465

1466



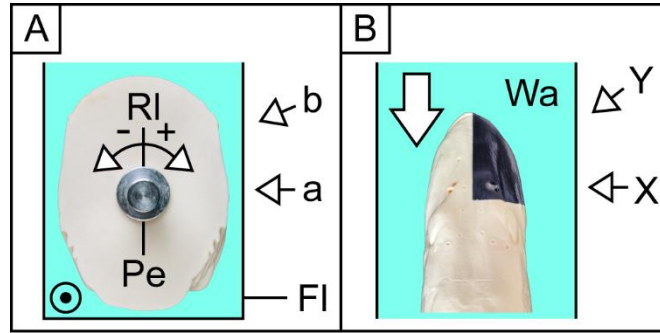
1467

1468

1469 **Fig. A.2.** Surface model of adult pike after smoothing of head mask. Asterisk: location of
1470 micro-CT artifact on rostral tip. Inset: magnified rostral surface. White disk: location on
1471 specimen of possible fragment of metal or glass. EN: Excurrent nostril; IN: incurrent nostril.

1472

1473



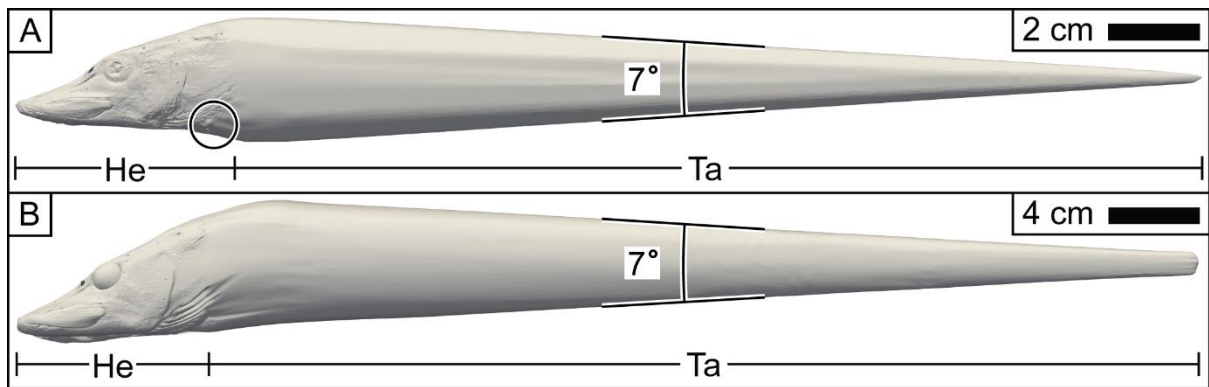
1474

1475

1476 **Fig. A.3.** Camera positions and roll in the dye visualisation experiments. (A) Transverse
1477 cross-section of flume, showing posterior face of plastic model of adult pike. (B) Dorsal
1478 aspect of flume/plastic model of adult pike. Circular symbol (A) and large arrow (B):
1479 direction of free-stream flow (out of page for circular symbol). Arrows a, b, X, and Y: camera
1480 positions. Images not to scale. Fl: Flume; Pe: aluminium peg; RI: roll angle; Wa: water.

1481

1482



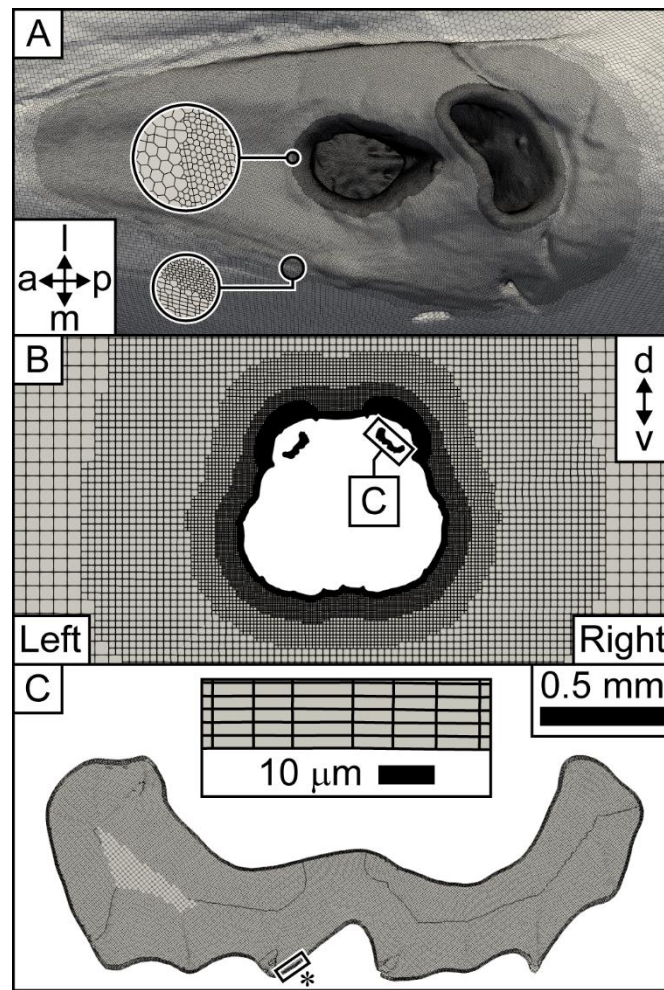
1483

1484

1485 **Fig. A.4.** CFD models of (A) juvenile and (B) adult pike. Circle: removed pectoral fin. He:

1486 Head; Ta: tapered extension ('tail').

1487



1489

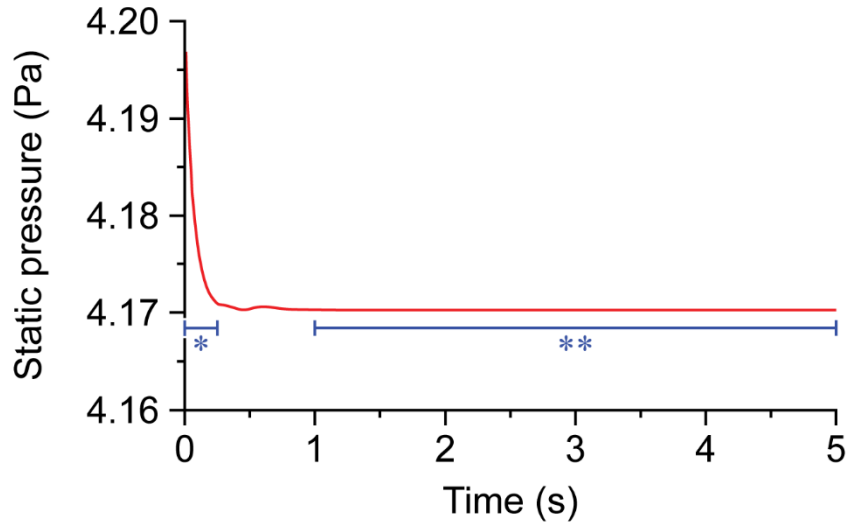
1490

1491 **Fig. A.5.** CFD mesh of juvenile pike. (A) Refinement of mesh on model surface, nasal region
 1492 (superior view). Large circles: magnified border (small circles) at two stages of refinement,
 1493 with refinement increasing bottom to top. (B) Transverse cross-section through mesh (same
 1494 cross-section as in Fig. 2A). (C) Transverse cross-section through nasal passage. Inset in (C):
 1495 mesh next to olfactory sensory surface (asterisked box, main image). Scale bars in (A) and
 1496 (B) and labels in all images deliberately omitted to allow reader to see mesh. a: Anterior; d:
 1497 dorsal; l: lateral; m: medial; p: posterior; v: ventral.

1498

1499

1500



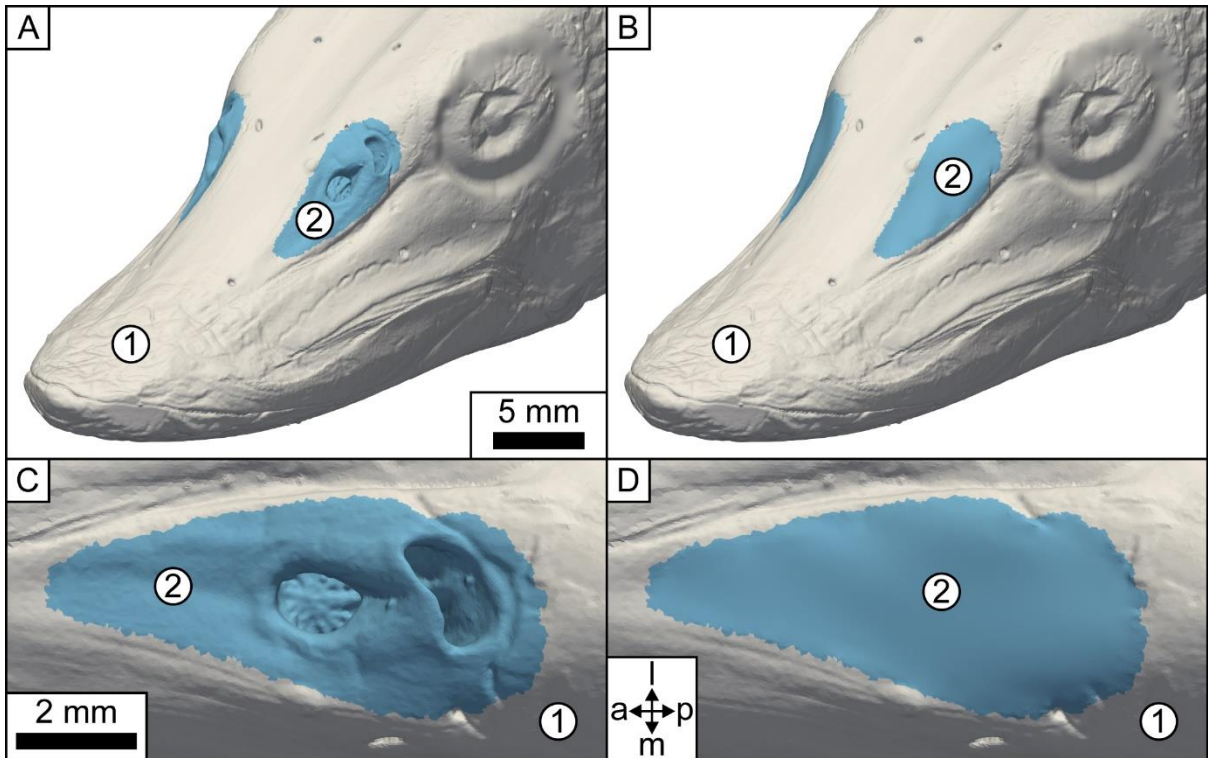
1501

1502

1503 **Fig. A.6.** Variation in static pressure in transient CFD simulation of model of juvenile pike
1504 (yaw 0°). Static pressure monitored in the centre of the right incurrent nostril. Red line:
1505 variation in static pressure. Blue line/asterisk: time taken for nasal chamber to be flushed
1506 once (steady-state simulation). Blue line/double asterisk: period over which the variation in
1507 static pressure at the monitoring point is $< 0.03\%$ of the average static pressure at that point
1508 over the same period.

1509

1510



1511

1512

1513

1514

1515

1516

1517

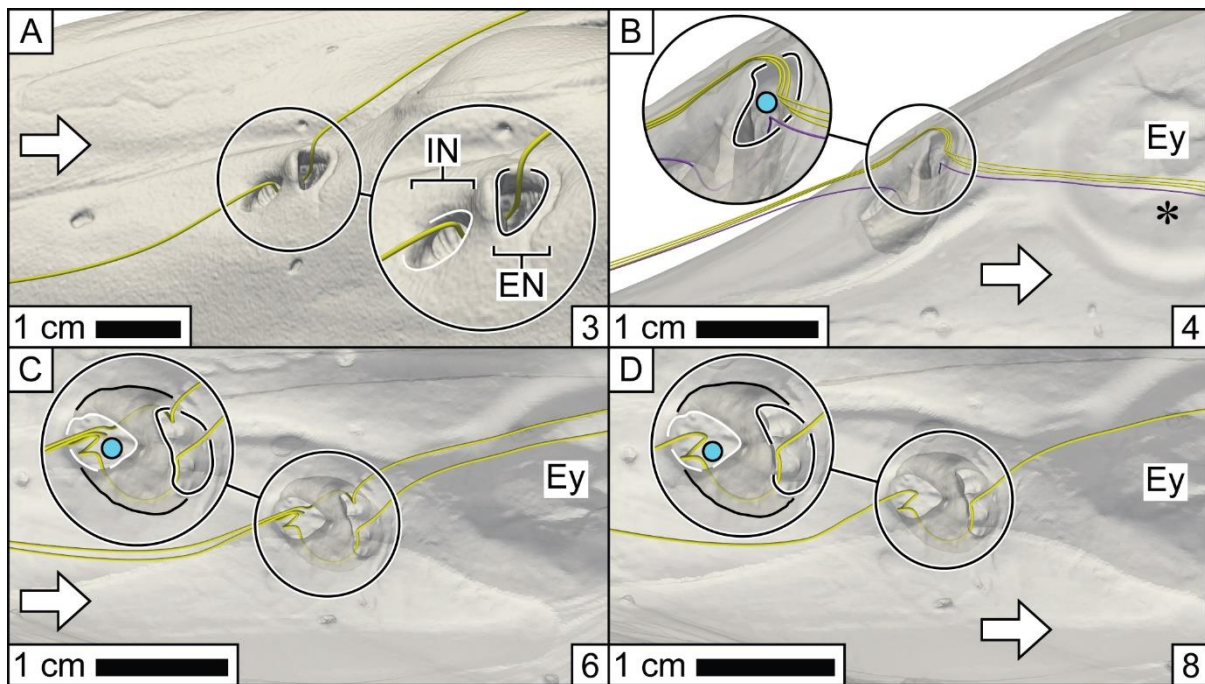
1518

1519

1520

Fig. A.7. CFD models of juvenile pike used for drag measurements. (A) Head of ‘wild type’ model (nasal regions unaltered). (B) Head of ‘mutant’ model (nostrils and nasal chamber of each nasal region replaced by a continuous surface). (C) and (D): Nasal region of wild type and mutant model, respectively (superior view). Numbers indicate the regions for which drag forces were measured: 1) head (white; includes tail); 2) nasal region (blue). Scale bars in (A) and (C) also apply to (B) and (D), respectively. The CFD models of the adult pike were partitioned in the same way. a: Anterior; l: lateral; m: medial; p: posterior.

1521



1522

1523

1524

1525

1526

1527

1528

1529

1530

1531

1532

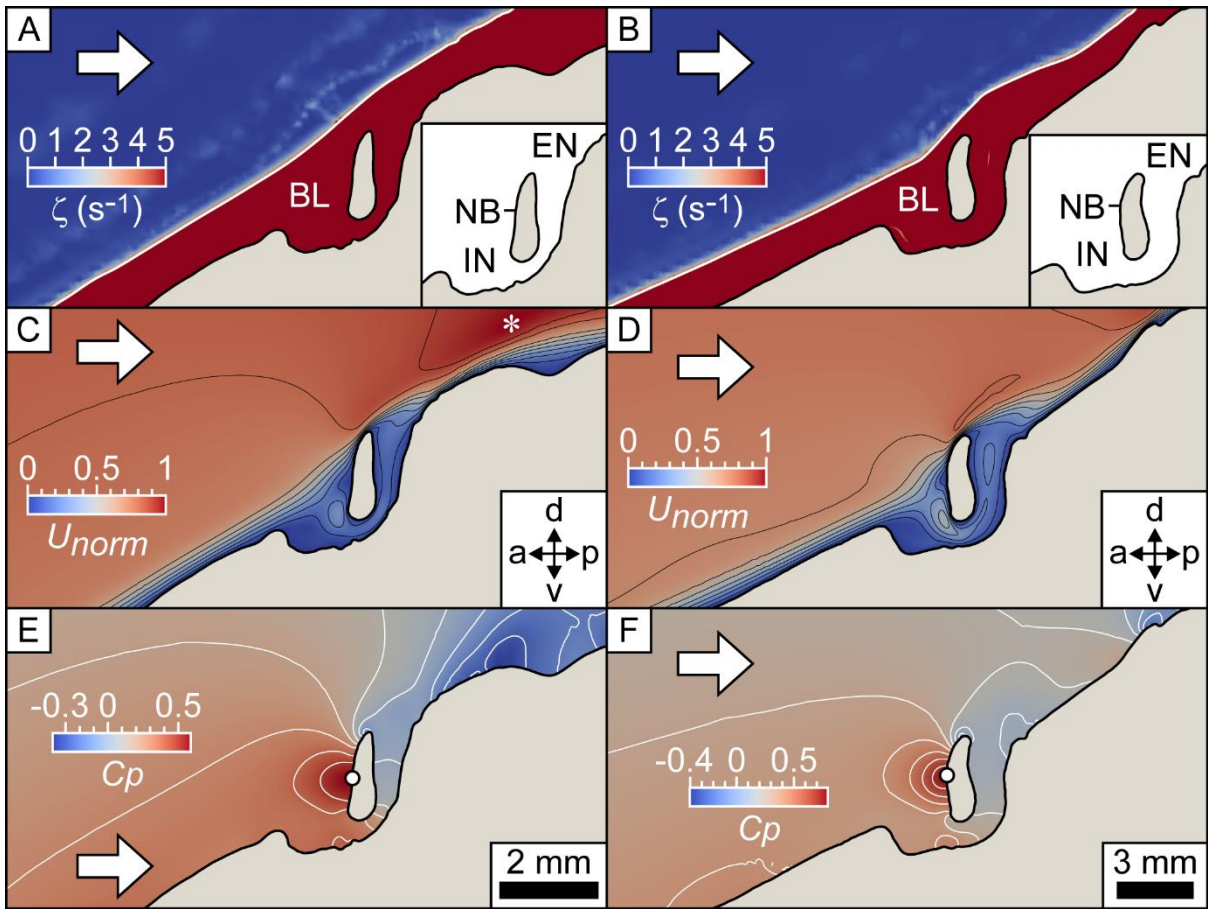
1533

1534

1535

1536

Fig. A.8. Correspondence of CFD-generated streamlines to olfactory flow in the plastic models of the pike. The plastic models are represented by surface models. Streamline(s) (tubes) correspond to dye behaviour in: (A) Video clip 3; (B) Video clip 4; (C) Video clip 6; and (D) Video clip 8 (video clip identified by number in box in each panel). (A) *Left* nasal region, adult pike; (B) – (D): nasal region, juvenile pike. (A): Dorsal aspect. (B): Lateral aspect. (C) and (D): Superior views. Insets: magnified nasal regions. Black lines in insets (C) and (D): extent of nasal chamber. Model in (B) – (D) at 50 % opacity, to match translucent right nasal region of plastic model. Scale bars refer to the size of the *plastic* models. Blue streamline in (B): flow passing through nasal chamber. Yellow streamlines in (B): flow participating in excurrent vortex. Arrow: direction of free-stream flow. Blue disk: vortex. Asterisk: (blue) streamline passing over eye. EN: Excurrent nostril (black on white lines); Ey: eye; IN: incurrent nostril (white lines).



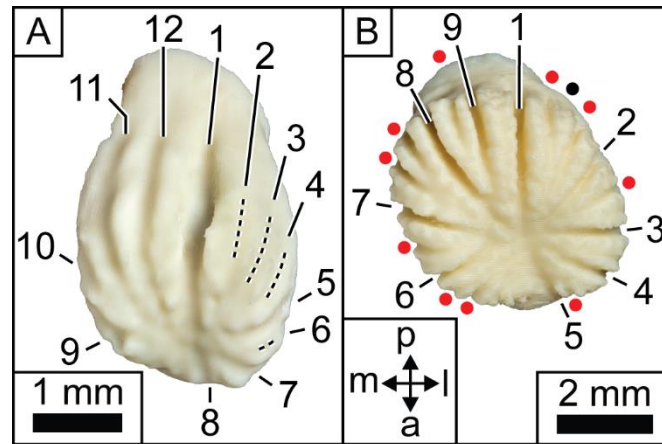
1538

1539

1540 **Fig. A.9.** Sagittal slices through CFD mesh in nasal region of juvenile (A, C and E) and adult
 1541 (B, D and F) pike. (A) and (B): Boundary layer, as defined by vorticity (ζ). White line: outer
 1542 limit of boundary layer. Insets: key parts of nasal region. (C) and (D): Flow speed (U_{norm}),
 1543 normalised to the maximum speed in each slice (asterisk in C). Black lines: contours of equal
 1544 speed. (E) and (F): pressure coefficients (C_p). White disk: maximum C_p . White lines:
 1545 isobars. Scale bar in (E) also applies to (A) and (C); scale bar in (F) also applies to (B) and
 1546 (D). Arrow: direction of free-stream flow. a: Anterior; BL: boundary layer; d: dorsal; EN:
 1547 excurrent nostril; IN: incurrent nostril; NB: nasal bridge; p: posterior; v: ventral.

1548

1549



1550

1551

1552 **Fig. A.10.** Plastic models of nasal volumes of pike. Ventral aspects. Nasal folds and sensory
1553 channels are represented by troughs and ridges, respectively. (A) Juvenile pike. Numbers:
1554 nasal folds. Dashed lines: locations (where not clear) of nasal folds. (B) Adult pike. Numbers:
1555 type I nasal folds (nomenclature according to Holl, 1965). Red disk: type II nasal fold. Black
1556 disk: type III nasal fold. Although the plastic models are larger than life, the scale bars refer
1557 to life-sized nasal volumes. a: Anterior; l: lateral; m: medial; p: posterior.

1558